Astronomy & Astrophysics

Excited OH$^+$, H$_2$O$^+$, and H$_3$O$^+$ in NGC 4418 and Arp 220*

E. González-Alfonso[1], J. Fischer[2], S. Bruderer[3], H. S. P. Müller[4], J. Graciá-Carpio[3], E. Sturm[3], D. Lutz[3],
A. Poglitsch[3], H. Feuchtgruber[3], S. Veilleux[5,6], A. Contursi[3], A. Sternberg[7], S. Hailey-Dunsheath[8], A. Verma[9],
N. Christopher[9], R. Davies[3], R. Genzel[3], and L. Tacconi[3]

[1] Universidad de Alcalá de Henares, Departamento de Física y Matemáticas, Campus Universitario, 28871 Alcalá de Henares,
  Madrid, Spain
  e-mail: eduardo.gonzalez@uah.es
[2] Naval Research Laboratory, Remote Sensing Division, 4555 Overlook Ave SW, Washington, DC 20375, USA
[3] Max-Planck-Institute for Extraterrestrial Physics (MPE), Giessenbachstraße 1, 85748 Garching, Germany
[4] I. Physikalisches Institut, Universität zu Köln, Zülpicher Str. 77, 50937 Köln, Germany
[5] Department of Astronomy, University of Maryland, College Park, MD 20742, USA
[6] Astroparticle Physics Laboratory, NASA Goddard Space Flight Center, Code 661, Greenbelt, MD 20771 USA
[7] Sackler School of Physics & Astronomy, Tel Aviv University, 69978 Ramat Aviv, Israel
[8] California Institute of Technology, Mail Code 301-17, 1200 E. California Blvd., Pasadena, CA 91125, USA
[9] University of Oxford, Oxford Astrophysics, Denys Wilkinson Building, Keble Road, Oxford, OX1 3RH, UK

ABSTRACT

We report on *Herschel*/PACS observations of absorption lines of OH$^+$, H$_2$O$^+$ and H$_3$O$^+$ in NGC 4418 and Arp 220. Excited lines of OH$^+$ and H$_2$O$^+$ with E_{lower} of at least 285 and ~200 K, respectively, are detected in both sources, indicating radiative pumping and location in the high radiation density environment of the nuclear regions. Abundance ratios OH$^+$/H$_2$O$^+$ of 1−2.5 are estimated in the nuclei of both sources. The inferred OH$^+$ column and abundance relative to H nuclei are $(0.5−1) \times 10^{16}$ cm^{-2} and ~2×10^{-8}, respectively. Additionally, in Arp 220, an extended low excitation component around the nuclear region is found to have OH$^+$/H$_2$O$^+$ ~ 5−10. H$_3$O$^+$ is detected in both sources with N(H$_3$O$^+$) ~ $(0.5−2) \times 10^{16}$ cm^{-2}, and in Arp 220 the pure inversion, metastable lines indicate a high rotational temperature of ~500 K, indicative of formation pumping and/or hot gas. Simple chemical models favor an ionization sequence dominated by H$^+$ → O$^+$ → OH$^+$ → H$_2$O$^+$ → H$_3$O$^+$, and we also argue that the H$^+$ production is most likely dominated by X-ray/cosmic ray ionization. The full set of observations and models leads us to propose that the molecular ions arise in a relatively low density ($\gtrsim 10^4$ cm^{-3}) interclump medium, in which case the ionization rate per H nucleus (including secondary ionizations) is $\zeta > 10^{-13}$ s^{-1}, a lower limit that is several $\times 10^2$ times the highest current rate estimates for Galactic regions. In Arp 220, our lower limit for ζ is compatible with estimates for the cosmic ray energy density inferred previously from the supernova rate and synchrotron radio emission, and also with the expected ionization rate produced by X-rays. In NGC 4418, we argue that X-ray ionization due to an active galactic nucleus is responsible for the molecular ion production.

Key words. line: formation – line: identification – ISM: abundances – galaxies: ISM – infrared: galaxies – molecular processes

1. Introduction

Observations of O-bearing molecular ions are powerful probes of the oxygen chemistry and related physical processes in the interstellar medium. The formation of OH$^+$, H$_2$O$^+$, and H$_3$O$^+$ can be initiated by cosmic ray and/or X-ray ionization of H and H$_2$ (e.g. Herbst & Klemperer 1973; Maloney et al. 1996), and hence their abundances are sensitive to the cosmic ray and X-ray fluxes that permeate the observed environments. Significant amounts of molecular ions can also be formed in the surfaces of photodissociation regions (PDRs) (Sternberg & Dalgarno 1995). The OH$^+$/H$_2$O$^+$ and OH$^+$/H$_3$O$^+$ abundance ratios are sensitive to the molecular fraction and to the fractional ionization, as the destruction paths for the three species are dominated by dissociative recombination (H$_3$O$^+$) and reactions with H$_2$ (OH$^+$ and H$_2$O$^+$; Gerin et al. 2010; Neufeld et al. 2010). In environments with T < 250 K, these are the intermediate species for the main

gas-phase production route of OH and H$_2$O, which are abundant species in the nuclei of some (ultra)luminous infrared galaxies ((U)LIRGs).

The successful launch and operation of the *Herschel* Space Observatory and its instruments have allowed the observation of O-bearing molecular ions in both galactic and extragalactic sources. In the Milky Way, and following the first detection of OH$^+$ towards Sgr B2 with APEX (Wyrowski et al. 2010), the ground-state lines of OH$^+$ and H$_2$O$^+$ have been observed in absorption toward a number of star-forming regions with high submillimeter continua, mainly tracing intervening diffuse/translucent clouds with low H$_2$ fraction (Ossenkopf et al. 2010; Gerin et al. 2010; Neufeld et al. 2010). The ground-state lines of both species have also been detected in the Orion BN/KL outflow, though still in absorption against the continuum (Gupta et al. 2010), and toward the high-mass star forming region AFGL 2591, also indicating low excitation for both hydrides (Bruderer et al. 2010b). Most of the Galactic OH$^+$ and H$_2$O$^+$ detections essentially sample low-excitation gas and are thought to be generated by the cosmic ray field in our galaxy

(Ossenkopf et al. 2010; Gerin et al. 2010; Neufeld et al. 2010; Hollenbach et al. 2012). The more stable H_3O^+ was first detected in the Sgr B2 molecular cloud complex near the Galactic center (Wootten et al. 1991), and further mapped with APEX in the same region (van der Tak et al. 2006) through the non-metastable $3_2^+ - 2_2^-$ submillimeter line at 365 GHz. Recently, high-lying lines of H_3O^+ from metastable levels have been detected in Sgr B2 by Lis et al. (2012), who suggested that the excitation could be due to formation pumping in X-ray irradiated gas.

The situation in luminous extragalactic sources is different in some aspects. While the ground-state transition of ortho-H_2O^+ has been detected in absorption in M82 (Weiß et al. 2010), the ground-state OH^+ and H_2O^+ lines have been detected in emission in Mrk 231, probably indicating a combination of high excitation conditions and high ionization rates that are plausibly tracing X-ray dominated regions (XDRs) due to the active galactic nucleus (AGN; van der Werf et al. 2010) or the high cosmic ray intensities suggested to be present in ULIRGs (Papadopoulos 2010). From ISO observations, hints of OH^+ absorption at ~ 153 μm from the first excited rotational level were previously reported in the ULIRGs Arp 220 (González-Alfonso et al. 2004, hereafter G-A04), and Mrk 231 (González-Alfonso et al. 2008), but the absorption in Arp 220 was mostly ascribed to NH. Recently, Rangwala et al. (2011, hereafter R11) have reported the detection of the ground-state OH^+ and o-H_2O^+ fine-structure components in absorption toward Arp 220, as well as two emission lines of H_2O^+ with excited lower levels. On the other hand, the H_3O^+ $3_2^+ - 2_2^-$ submillimeter line has also been detected in Arp 220 (van der Tak et al. 2008, hereafter vdT08) and other nearby galaxies (Aalto et al. 2011).

We report in this work on the *Herschel*/PACS detection of excited OH^+, H_2O^+, and H_3O^+ in both Arp 220 and NGC 4418. In a recent study (González-Alfonso et al. 2012, hereafter Paper I), we have reported on the *Herschel*/PACS observations of these two sources in H_2O, $H_2^{18}O$, OH, ^{18}OH, HCN, and NH_3, together with a quantitative analysis in which a deconvolution of the continuum into several components enabled us to derive the column densities and abundances of these species associated with each of the components. A chemical dichotomy was found in Paper I: on the one hand, the nuclear regions of both galaxies have high H_2O abundances ($\sim 10^{-5}$), and high HCN and NH_3 column densities, indicating a chemistry characterized by high T_{gas}, T_{dust}, and high density, where the release of molecules from grain mantles to the gas phase has occurred (through evaporation in "hot core" chemistry and sputtering in shocks). On the other hand, the high OH abundance found in both sources, with OH/$H_2O \sim 0.5$, appears to indicate the occurrence of photoprocesses due to X-rays and/or the effects of cosmic rays. This second aspect of the chemistry is further studied in this paper from the observed O-bearing molecular cations detected in the *Herschel*/PACS spectra of both sources. The paper is organized as follows: the observations are presented in Sect. 2; column densities and abundances are inferred in Sect. 3; chemical models are presented and compared with observations in Sect. 4; the inferred important processes are discussed in Sect. 5, and the main conclusions are listed in Sect. 6. As in Paper I, we adopt distances to Arp 220 and NGC 4418 of 72 and 29 Mpc, and redshifts of $z = 0.0181$ and 0.00705, respectively.

2. Observations and results

The full, high resolution, PACS spectra of NGC 4418 and Arp 220, were observed as part of the guaranteed-time key program SHINING on July 27th and February 27th (2010),

respectively[1]. The data reduction was done using the standard PACS reduction and calibration pipeline (ipipe) included in HIPE 5.0 975. For the final calibration, the spectrum was normalized to the telescope flux and recalibrated with a reference telescope spectrum obtained from Neptune observations. Further details of the data reduction are given in Graciá-Carpio et al. (2011), Sturm et al. (2011), and Paper I.

The PACS spectrum of Arp 220 in Paper I was corrected in both flux and wavelength calibration due to the effects of sub-spaxel pointing errors. Following newly made software corrections to the *Herschel* pointing star catalogue and the star-tracker x and y focal lengths, a second full spectrum of Arp 220 was taken by the Observatory to assess the improvement to *Herschel*'s pointing. Although the baseline of the new spectrum is of higher quality, general agreement with our corrected original spectrum was found in both flux and wavelength calibration. The data shown here are mostly an average of the two observations, except for some ranges where the new data set yields a more reliable baseline.

Spectroscopic parameters of OH^+, H_2O^+, and H_3O^+ used for line identification and radiative transfer modeling were mostly taken from the spectral line catalogs of the CDMS (Müller et al. 2001, 2005) and JPL (Pickett et al. 1998), and are included in Table 1, together with the equivalent widths (W_{eq}) and fluxes of the detected lines. The wavelength uncertainties tabulated in the catalogs are significantly lower than the PACS spectral resolution. Energy level diagrams for the three cations are shown in Fig. 1, where the solid red arrows indicate the detected transitions in at least one of the sources.

2.1. OH^+

Owing to the electronic spin $S = 1$, all rotational levels of OH^+ except the ground $N = 0$ state are split into 3 fine-structure levels with total angular momentum $J = N-1, N, N+1$ (Fig. 1)[2]. Of the six allowed fine-structure transitions between excited rotational levels, the three with $\Delta J = \Delta N$ are the strongest. Line spectroscopic parameters of OH^+ were taken from the CDMS, and were derived by Müller et al. (2005). In that work, the $N = 1-0$ transition frequencies from Bekooy et al. (1985) were fit together with additional infrared data. A dipole moment of 2.256 D was taken from an ab initio study (Werner et al. 1983).

Figure 2 shows the observed spectra around the OH^+ lines in NGC 4418 (upper histograms) and Arp 220 (lower histograms). The spectra around the positions of the $2_J \leftarrow 1_{J'}$ lines, with $E_{lower} \approx 50$ K, are displayed in panels a–c. The strongest $2_3 \leftarrow 1_2$ at ≈ 153 μm is partially blended with NH, but the $2_2 \leftarrow 1_1$ is free from contamination and clearly detected in both sources. In Arp 220, the 153 μm absorption appears to be dominated by OH^+ rather than by NH, in contrast with the initial estimate by González-Alfonso et al. (2004) based on ISO data. The $2_1 \leftarrow 1_0$ at ≈ 148.7 μm is also well detected, and the intrinsically weaker $2_1 \leftarrow 1_1$ (158.4 μm) and $2_2 \leftarrow 1_2$ (147.8 μm) lines are (marginally) detected in NGC 4418 but still very strong in Arp 220. There is in addition an apparent red-shifted wing in the NH $2_3 \leftarrow 1_2$ spectrum of Arp 220, detected in both data sets, which coincides with the position of the intrinsically weak OH^+
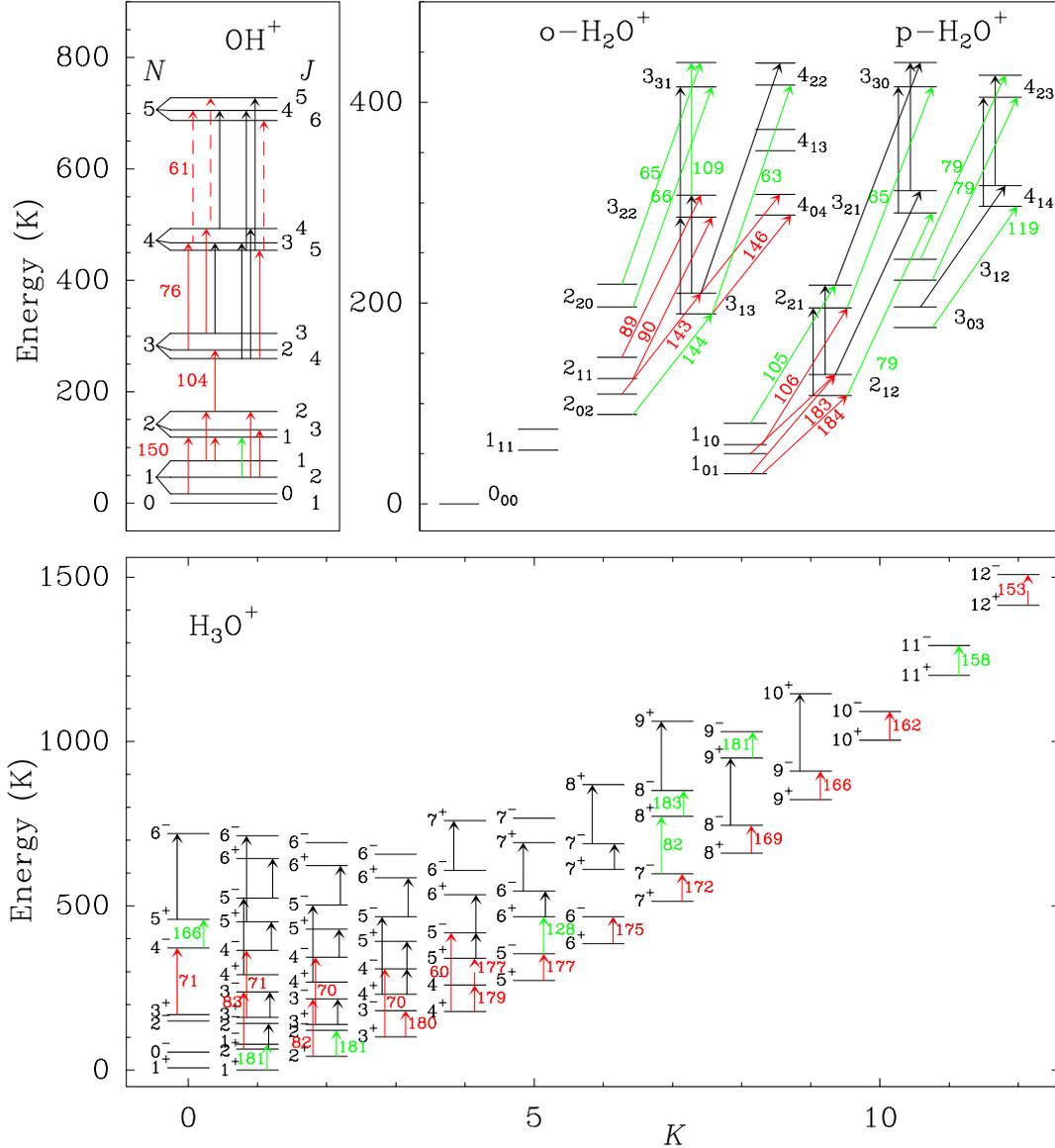
Fig. 1. Energy level diagrams of OH^+, H_2O^+, and H_3O^+, showing with arrows the transitions that lie within the PACS range; colored numbers indicate round-off wavelengths in μm. The fine-structure splitting of the OH^+ and H_2O^+ levels is out of scale. Solid-red arrows mark the lines detected in NGC 4418 and/or Arp 220; dashed-red arrows indicate marginal detection in any of the sources; green arrows indicate blended lines, and black arrows show undetected lines.

$2_1 \leftarrow 1_2$ transition. As shown below (Sect. 2.3), however, this wing feature is most probably due to the very excited $12^-_{12} \leftarrow 12^+_{12}$ line of H_3O^+.

Most $3_J \leftarrow 2_{J'}$ lines at $\sim 100\,\mu m$ lie within the gap between the green ($\lambda < 100\,\mu m$) and red ($\lambda > 100\,\mu m$) bands of PACS and are not observable, except for the $3_2 \leftarrow 2_2$ transition at $103.9\,\mu m$ shown in Fig. 2d. The line in NGC 4418 is close to the edge of the red band where the spectral noise is high, but in Arp 220 a clear spectral feature is detected at the expected wavelength. The line, however, is blended with the H_2O $6_{15} \leftarrow 6_{06}$ transition (Paper I), which may account for some of the observed absorption.

The three strongest $4_J \leftarrow 3_{J'}$ lines at $76 - 76.5\,\mu m$ are clearly detected in both sources (Fig. 2e), indicating a high-excitation component in the transient OH^+. It is worth noting that while the $2_J \leftarrow 1_{J'}$ lines are stronger in Arp 220, the more excited $4_J \leftarrow 3_{J'}$ lines are slightly deeper in NGC 4418, resembling the behavior found for other species like H_2O, OH, HCN, and NH_3

(Paper I). The $4_J \leftarrow 3_{J'}$ lines still have slightly higher equivalent widths in Arp 220 (Table 1) owing to the broader line profiles in this source. The line opacities of the fine-structure components are $\tau \propto \lambda^3 g_u A_{ul}$ if the lower levels are populated according to their degeneracies, and then $\tau_{4_5-3_4}:\tau_{4_4-3_3}:\tau_{4_3-3_2} = 1:0.77:0.58$. These are expected to be the ratios of the line equivalent widths (W_{eq}) if the three components are optically thin. In Arp 220, the observed W_{eq} ratios are $1:(0.69 \pm 0.11):(0.53 \pm 0.10)$ (Table 1), consistent with optically thin absorption. In NGC 4418 they are $1:(1.2 \pm 0.6):(1.0 \pm 0.5)$, compatible within the uncertainties with both optically thin and saturated absorption.

In NGC 4418, some marginal features around $61\,\mu m$ roughly coincide with the positions of the OH^+ $5_J \leftarrow 4_{J'}$ lines (Fig. 2f). However, the feature associated with the intrinsically strongest $5_6 \leftarrow 4_5$ component is relatively weak and shifted in wavelength by $0.015\,\mu m$, shedding doubt on this tantalizing identification. In Arp 220, this part of the spectrum was affected by instrumental problems and is not shown.
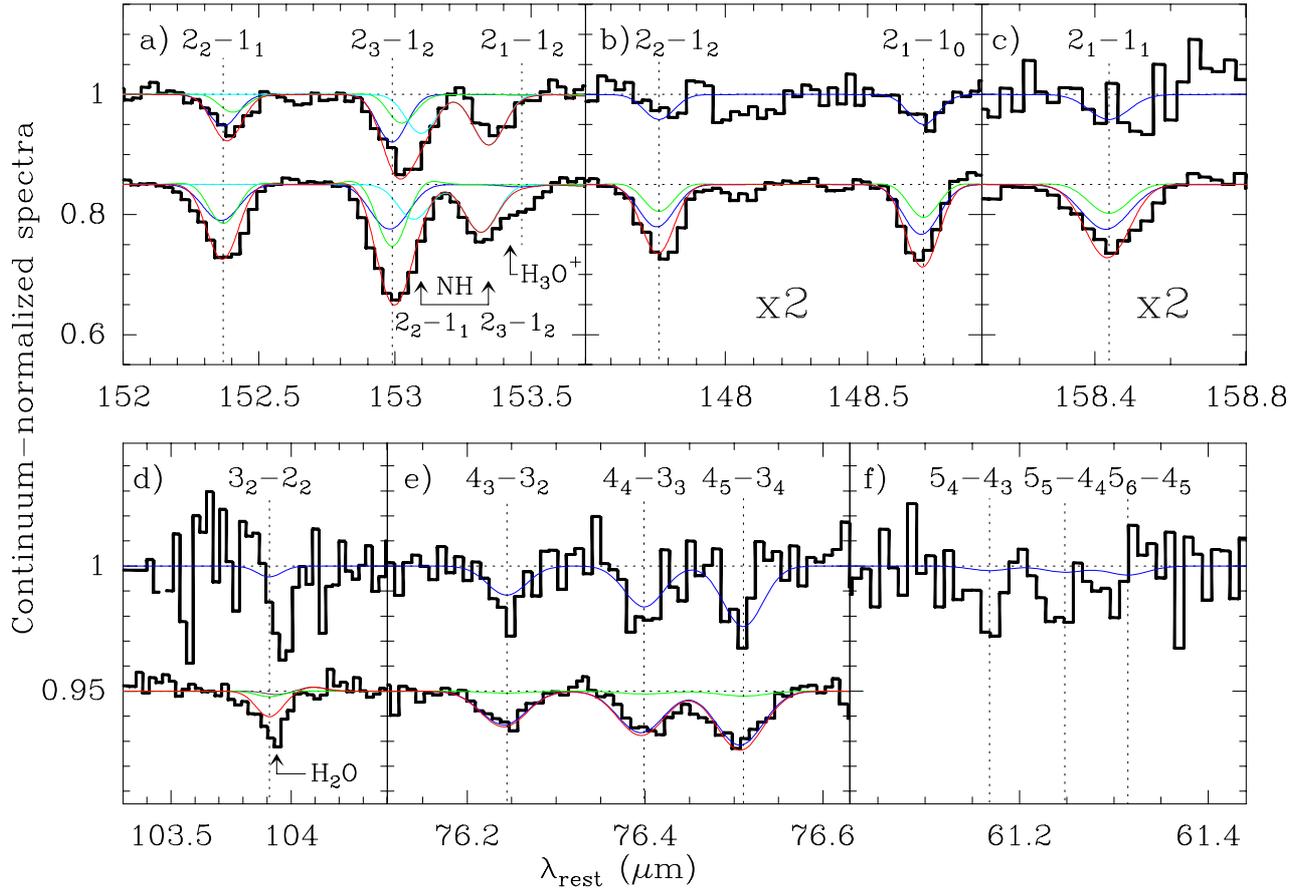
Fig. 2. Continuum-normalized spectra around the OH$^+$ lines in NGC 4418 (upper histograms) and Arp 220 (lower histograms). The dotted vertical lines indicate the rest wavelengths of the transitions for the nominal redshifts of $z = 0.00705$ (NGC 4418) and 0.0181 (Arp 220). The spectra in panels **b)** and **c)** have been scaled by a factor 2. (Potential) contamination by other species (NH in panel **a)** and H_2O in **d)**) is also indicated. The marginal $5_J - 4_{J'}$ lines in **f)** correspond to NGC 4418; this part of the spectrum is not available in Arp 220. Blue lines show model fits for OH$^+$ in the nuclear components of both NGC 4418 and Arp 220, the green lines show the model fit for OH$^+$ in the extended components of both sources, and the light-blue lines in **a)** are model fits for NH; red is total.

2.2. H_2O^+

The asymmetric H_2O^+ also has fine-structure splitting of the rotational levels producing doublets ($S = 1/2$) and yielding a very rich spectrum in the far-infrared domain (Fig. 1). Predictions of the rotational spectrum were taken from the CDMS. The CDMS data were based on extrapolated zero-field frequencies in Mürtz et al. (1998), the derived $N = 1-0$ transition frequencies based on Strahan et al. (1986), and additional rovibrational (infrared) transitions and ground state data from electronic spectra. HIFI observations of the $N = 1_{10}-1_{01}$ transition frequencies above 600 GHz toward Sgr B2(M) reported by Schilke et al. (2010) are compatible with the transition frequencies in the CDMS, although these lines lie outside our accessible frequency range. A ground state dipole moment of 2.398 D was calculated ab initio by Weis et al. (1989).

As shown in Fig. 1, most low-lying lines of H_2O^+ are blended with lines of other species, but some of them lie in free windows (Fig. 3). Very prominent is the ground-state p-H_2O^+ $2_{12} \leftarrow 1_{01}$ transition at 183–184 μm in Arp 220, with the three fine-structure components clearly identified in the spectrum. This transition is not detected in NGC 4418. In Arp 220, the observed line strengths strongly decrease with increasing E_{lower}, indicating that the ground-state p-H_2O^+ lines arise in low excitation gas. The opacity ratios of these components are $\tau_{5/2-3/2}$:$\tau_{3/2-1/2}$:$\tau_{3/2-3/2}$ = 1:0.55:0.12, so the observed

W_{eq} ratios of 1:(0.65 ± 0.07):(0.30 ± 0.05) (Table 1) suggest line saturation effects in at least the strongest 5/2–3/2 component. For $\sigma_v = 60$ km s^{-1}, this component attains an optical depth of unity with a column of $N(p-H_2O^+) \approx 5 \times 10^{14}$ cm^{-2}. The line absorbs only $\approx$15% of the continuum, likely indicating some spectral dilution and a low covering factor of the continuum.

The two prominent features at 104.7–105 μm in both NGC 4418 and Arp 220 are most probably due to NH$_2$. The feature at 143.8 μm may be contaminated by C_3. In Arp 220, the excited $2_{21} \leftarrow 1_{10}$, $3_{13} \leftarrow 2_{02}$, $3_{22} \leftarrow 2_{11}$, and $4_{04} \leftarrow 3_{13}$ lines of H_2O^+, with E_{lower} up to 190 K, are clearly detected, but in NGC 4418 only the high-lying $3_{22} \leftarrow 2_{11}$ transition shows measurable absorption. Detection of the $4_{04} \leftarrow 3_{13}$ transition in NGC 4418 is questionable, as the spectral features associated with the 9/2–7/2 and 7/2–5/2 components are either too narrow or shifted (Fig. 3e).

2.3. H_3O^+

H_3O^+ and NH$_3$ are isoelectronic and spectroscopically similar: both are oblate symmetric top rotors, have a double-minimum potential such that inversion takes place between the two equivalent minima, and have *ortho* ($K = 3n$) and *para* ($K \neq 3n$) modifications. Figure 1 shows the energy level diagram for H_3O^+. Owing to the $\Delta K = 0$ selection rule for all radiative transitions, the $J = K$ levels in the lower tunneling state cannot

Table 1. Line equivalent widths and absorption fluxes.

Line	E_{lower} (K)	λ (μm)	A_{ul} (s^{-1})	NGC 4418 $W_{\text{eq}}{}^a$ (km s^{-1})	NGC 4418 Flux^a (10^{-21} W cm^{-2})	Arp 220 $W_{\text{eq}}{}^a$ (km s^{-1})	Arp 220 Flux^a (10^{-21} W cm^{-2})
OH$^+$ 2_1-1_0	43.6	148.696	0.10	6.7(1.8)	0.79(0.21)	17.8(0.9)	10.0(0.5)
OH$^+$ 2_3-1_2	46.6	152.989	0.18	b	b	b	b
OH$^+$ 2_2-1_2	46.6	147.768	0.048	3.9(1.6)	0.47(0.19)	20.7(1.2)	12.0(0.7)
OH$^+$ 2_2-1_1	49.6	152.369	0.14	19.5(2.1)	2.1(0.2)	45.3(1.3)	24.6(0.7)
OH$^+$ 2_1-1_1	49.6	158.437	0.071	5.9(3.0)	0.6(0.3)	19.8(1.1)	9.6(0.5)
OH$^+$ 4_5-3_4	281.9	76.510	1.6	3.1(0.7)	1.6(0.4)	5.8(0.4)	10.6(0.7)
OH$^+$ 4_3-3_2	282.5	76.245	1.5	3.2(0.8)	1.6(0.4)	3.1(0.4)	5.7(0.7)
OH$^+$ 4_4-3_3	285.5	76.399	1.5	3.8(0.8)	1.9(0.4)	4.0(0.4)	7.4(0.7)
pH$_2$O$^+$ $2_{12}\frac{5}{2}-1_{01}\frac{3}{2}$	0.0	184.339	0.086	<4.8	<0.25	47.6(2.1)	10.5(0.5)
pH$_2$O$^+$ $2_{12}\frac{3}{2}-1_{01}\frac{1}{2}$	0.1	182.915	0.073	<3.7	<0.21	30.8(2.1)	7.5(0.4)
pH$_2$O$^+$ $2_{12}\frac{3}{2}-1_{01}\frac{3}{2}$	0.0	182.640	0.016	<3.7	<0.21	14.5(1.6)	3.6(0.4)
pH$_2$O$^+$ $2_{21}\frac{5}{2}-1_{10}\frac{3}{2}$	29.1	105.742	0.46	7.6(2.3)	2.1(0.6)	6.2(0.8)	7.7(1.0)
pH$_2$O$^+$ $2_{21}\frac{3}{2}-1_{10}\frac{1}{2}$	30.4	104.719	0.39	b	b	b	b
oH$_2$O$^+$ $3_{13}\frac{7}{2}-2_{02}\frac{5}{2}$	89.1	143.813	0.18	5.2(2.5)	0.65(0.31)	22.6(1.1)	14.0(0.7)
oH$_2$O$^+$ $3_{13}\frac{5}{2}-2_{02}\frac{3}{2}$	89.3	143.270	0.17	<3.0	<0.38	8.3(0.9)	5.2(0.6)
oH$_2$O$^+$ $3_{22}\frac{7}{2}-2_{11}\frac{5}{2}$	125.0	89.590	0.59	7.2(2.3)	2.9(0.9)	10.2(0.7)	16.6(1.1)
oH$_2$O$^+$ $3_{22}\frac{5}{2}-2_{11}\frac{3}{2}$	125.9	88.978	0.57	5.4(1.6)	2.2(0.6)	2.2(1.1)	3.6(1.8)
oH$_2$O$^+$ $4_{04}\frac{9}{2}-3_{13}\frac{7}{2}$	189.2	145.917	0.16	4.4(0.8)	0.55(0.10)	2.0(0.5)	1.2(0.3)
oH$_2$O$^+$ $4_{04}\frac{7}{2}-3_{13}\frac{5}{2}$	189.8	146.217	0.15	4.7(0.8)	0.58(0.10)	5.5(0.6)	3.2(0.4)
oH$_3$O$^+$ $3_3^--3_3^+$	102.0	180.209	0.083	<3.9	<0.25	28(3)^c	8.5(1.0)^c
pH$_3$O$^+$ $4_4^--4_4^+$	179.0	178.994	0.091	<3.9	<0.27	12.7(1.3)	4.0(0.4)
pH$_3$O$^+$ $5_5^--5_5^+$	273.4	177.272	0.097	<6.0	<0.44	13.9(1.6)	4.4(0.5)
oH$_3$O$^+$ $6_6^--6_6^+$	385.1	175.063	0.10	<4.6	<0.38	18.6(1.3)	6.4(0.4)
pH$_3$O$^+$ $7_7^--7_7^+$	514.0	172.396	0.11	<3.4	<0.28	11.8(1.4)	4.2(0.5)
pH$_3$O$^+$ $8_8^--8_8^+$	660.1	169.303	0.12	d	d	13.7(1.2)	5.4(0.5)
oH$_3$O$^+$ $9_9^--9_9^+$	823.3	165.819	0.13	8.0(2.0)	0.71(0.18)	16.5(2.0)^e	6.9(0.8)^e
pH$_3$O$^+$ $10_{10}^--10_{10}^+$	1003.5	161.984	0.14	<3.7	<0.36	7.5(1.1)	3.3(0.5)
oH$_3$O$^+$ $12_{12}^--12_{12}^+$	1414.7	153.424	0.17			8.5(1.5)^f	4.5(0.8)^f
pH$_3$O$^+$ $5_4^--4_4^+$	179.0	60.164	0.49	5.8(2.0)	4.1(1.4)	5.5(1.2)	12.1(2.7)
oH$_3$O$^+$ $4_3^--3_3^+$	102.0	69.538	0.38	6.1(1.3)	3.7(0.8)	17.0(1.5)	33.6(2.9)
pH$_3$O$^+$ $4_2^--3_2^+$	139.3	70.254	0.63	<2.3	<1.4	5.4(0.7)	10.4(1.4)
pH$_3$O$^+$ $4_1^--3_1^+$	161.7	70.684	0.77	5.9(1.9)	3.5(1.1)	4.8(0.5)	9.1(1.0)
oH$_3$O$^+$ $4_0^--3_0^+$	169.1	70.827	0.81	8.0(2.0)	4.6(1.2)	7.7(0.8)	15.8(1.5)
pH$_3$O$^+$ $3_2^--2_2^+$	42.3	82.274	0.28	4.0(1.3)	1.8(0.6)	7.9(0.6)	13.8(1.0)
pH$_3$O$^+$ $3_1^--2_1^+$	64.7	82.868	0.44	<1.2	<0.6	13.1(0.7)	23.2(1.2)

Notes. $^{(a)}$ Numbers in parenthesis indicate 1σ uncertainties. $^{(b)}$ The line is strongly contaminated. $^{(c)}$ Contaminated by H$_2$O and CH (Fig. 4a). $^{(d)}$ Dominated by HCN (Paper I). $^{(e)}$ Contaminated by NH$_3$; the line flux in Arp 220 is estimated by subtracting the modeled NH$_3$ flux from the flux of the whole feature (Fig. 4g). $^{(f)}$ Tentative detection, at the wing of the NH 153 μm line (Figs. 2a and 4i).

be radiatively pumped and hence are metastable. They therefore will be "thermally" populated at a rotational temperature, T_{rot}, which reflects either T_{gas} or, if the formation-destruction rates are faster than the rate for collisional relaxation, the formation process characteristics (e.g. Bruderer et al. 2010a; Lis et al. 2012, see also Appendix B).

Spectroscopic data for H$_3$O$^+$ were taken from the JPL catalogue (Pickett et al. 1998). The entry was based on the recent analysis by Yu et al. (2009), who also presented some improved transition frequencies. The majority of the pure tunneling transition frequencies were reported by Verhoeve et al. (1989). A ground state dipole moment of 1.44 D was calculated ab initio by Botschwina et al. (1985). The antisymmetric[3] state is higher in energy by 1659 GHz (Yu et al. 2009) because of the low barrier

to linearity, and thus the pure inversion transitions of H$_3$O$^+$ lie in the far-IR domain (150−185 μm)[4].

The solid-red arrows in Fig. 1 indicate the H$_3$O$^+$ lines detected in Arp 220, and Fig. 4 presents the observed H$_3$O$^+$ spectra of NGC 4418 and Arp 220. In Arp 220, spectral features at the wavelengths of the H$_3$O$^+$ pure-inversion, metastable (hereafter PIMS) lines (panels a−i) are detected up to a lower level energy of $\approx$1400 K above the ground state (12_{12}^+), while none of these lines is detected in NGC 4418. The rotation-inversion (hereafter RI) lines lie at shorter wavelengths ($\lambda < 100\,\mu$m) and are shown in Fig. 4j−p. Four of them arise from non-metastable levels (Fig. 1), three of them from metastable levels (hereafter RIMS lines), and are detected within the lowest $K \leq 4$ ladders up to an energy of $\sim$200 K in both galaxies.

---

[3] The symmetric and antisymmetric states are here denoted with + and −, respectively.

[4] For NH$_3$, the antisymmetric state is higher in energy by 23.7 GHz and the pure-inversion transitions lie at centimeter wavelengths.
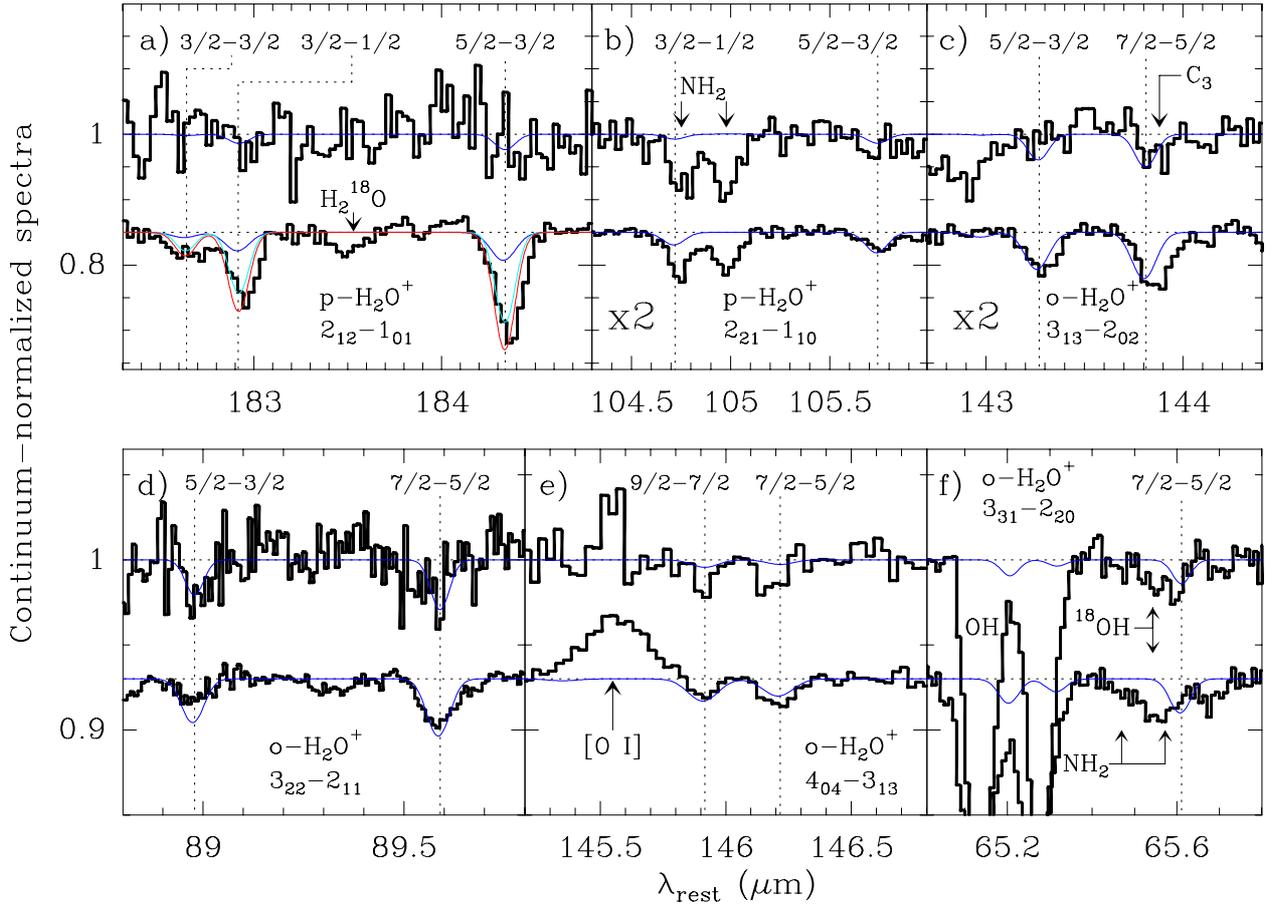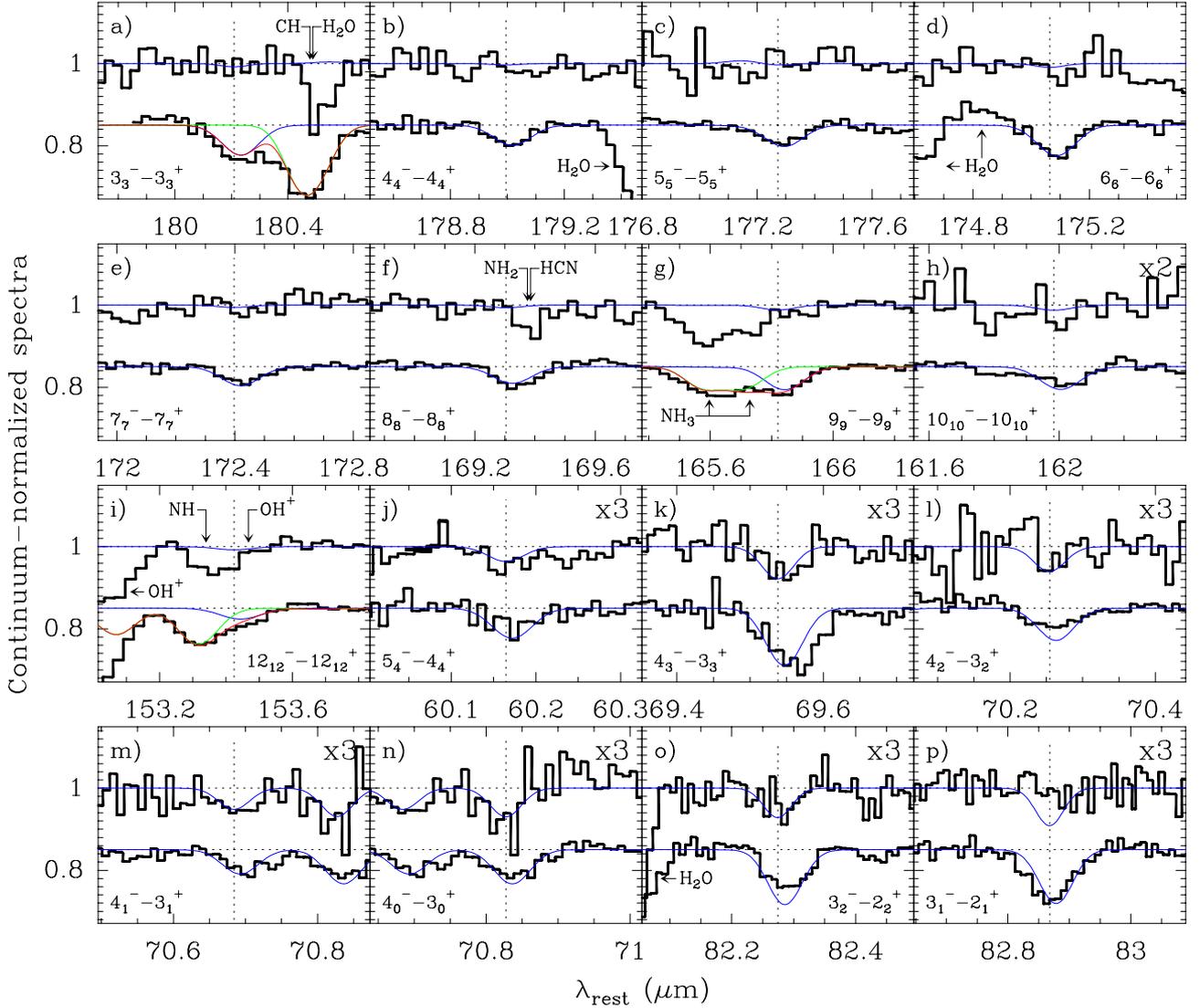
Fig. 3. Continuum-normalized spectra around the H_2O^+ lines in NGC 4418 (*upper histograms*) and Arp 220 (*lower histograms*). The dotted vertical lines indicate the rest wavelengths of the transitions for the nominal redshifts of $z = 0.00705$ (NGC 4418) and 0.0181 (Arp 220). The spectra in panels **b)** and **c)** have been scaled by a factor 2. Close features due to other species and potential contaminations are indicated. Dark blue and light blue lines show model fits; red is total.

The $1_1^- - 1_1^+$, $2_2^- - 2_2^+$, and $11_{11}^- - 11_{11}^+$ PIMS lines are contaminated by strong lines of CH, $H_2^{18}O$, and [C II], and are not shown. All features in Arp 220 are detected in both datasets. Close lines due to other species, as well as potential contaminations (panels f and i), are also indicated in Fig. 4. Based on the weakness of the HCN 19–18 line (Paper I), the HCN 20 − 19 line at 169.39 μm is not expected to strongly contaminate the H_3O^+ $8_8^- \leftarrow 8_8^+$ line, though some contribution from HCN is not ruled out (see below). Likewise, the nearby NH_2 $3_{30} \leftarrow 3_{21}$ 4−3 line is intrinsically weak, and NH_2 modeling that accounts for other detected NH_2 lines does not produce significant absorption at 169.38 μm. A broad feature is detected at 165.7 μm (panel g), which cannot be explained by only the NH_3 $3_2^- \leftarrow 2_2^+$ and $3_1^- \leftarrow 2_1^+$ lines (Paper I); thus strong absorption by ortho-H_3O^+ $9_9^- \leftarrow 9_9^+$ is inferred. The relatively weak H_3O^+ $10_{10}^- \leftarrow 10_{10}^+$ line is affected by an uncertain baseline, though the line is detected in both data sets. On the other hand, a line wing feature close to the NH $2_3 \leftarrow 1_2$ 153.35 μm line is detected, coinciding with both the ortho-H_3O^+ $12_{12}^- \leftarrow 12_{12}^+$ and the OH^+ $2_1 \leftarrow 1_2$ lines (153.47 μm, see also Fig. 2a). As mentioned earlier, the latter is also intrinsically weak, and modeling of the other OH^+ $2_J \leftarrow 1_{J'}$ lines (Sect. 3.4) yields negligible absorption in that component. Upon inspection of the CDMS and JPL catalogs, we have not found any other reliable candidate for the NH wing, which we tentatively ascribe to the very high-lying H_3O^+ line.

No potential contamination has been found for the RI lines. Contrary to the PIMS lines, some of these RI lines are detected

in NGC 4418. The non-metastable levels are populated through absorption of far-IR photons, and trace the local far-IR radiation density.

The PIMS and RIMS lines are observed in absorption against the strong far-IR continuum source of Arp 220, and their relative strengths probe T_{rot}. The population diagram of H_3O^+ is shown in Fig. 5, where the level columns have been calculated in the optically thin limit and by assuming that the H_3O^+ covers the whole continuum from Arp 220. Since the degeneracy of the ortho levels is twice that of the para levels, we expect a nearly continuous distribution for an ortho-to-para ratio of 1, as observed in the high-lying levels (crosses in Fig. 5). The distribution is roughly described with two values of T_{rot}, ~180 K up to the 5_5^+ level, and ~550 K for higher-lying levels. This is strikingly similar to that found by Lis et al. (2012) towards Sgr B2. The column of the 8_8^+ level ($E_l \approx 660$ K) appears to be higher than expected, suggesting some contamination by HCN at 169.4 μm (Fig. 4f). On the other hand, there are two metastable levels, the 3_3^+ and the 4_4^+, for which both PIMS and RIMS lines are available. In both levels, the columns derived from the RIMS lines are higher by a factor of ≈ 1.8 than those derived from the PIMS lines. Two main reasons can account for this: first, the level columns are calculated, as mentioned above, by assuming that the H_3O^+ covers the whole far-IR continuum, which is relatively cold (i.e. $S_{180}/S_{60} = 0.43$). If the H_3O^+ is absorbing a warmer continuum that is diluted within the observed SED (i.e. filled in by a cooler continuum source), the intrinsic equivalent width and column of

Fig. 4. Continuum-normalized spectra around the H$_3$O$^+$ lines in NGC 4418 (*upper histograms*) and Arp 220 (*lower histograms*). The dotted vertical lines indicate the rest wavelengths of the transitions for the nominal redshifts of $z = 0.00705$ (NGC 4418) and 0.0181 (Arp 220). Panels **a)**−**i)** show the pure inversion, metastable lines of H$_3$O$^+$, while panels **j)**−**p)** show the rotation-inversion lines at $\lambda < 100\,\mu$m. The spectra in panels **h)** and **j)**−**p)** have been scaled by a factor 2 and 3, respectively. The $1_1^- - 1_1^+$ and $2_2^- - 2_2^+$ lines at $\approx 181\,\mu$m are strongly contaminated by lines of CH and H$_2^{18}$O, and are not shown. Close features due to other species and potential contaminations are indicated. In panels **f)** and **i)**, the contamination by NH$_2$, HCN, and OH$^+$ is expected to be small (see text). The blue lines show the best-fit model for H$_3$O$^+$; the green lines in panels **g)** and **i)** show model fits for NH$_3$ and NH lines; red is the total.

the PIMS lines will be increased relative to those of the RIMS line, and both columns will be in better agreement. Therefore, the discrepancy probably indicates that the highly excited H$_3$O$^+$ covers only a fraction of the observed continuum, and that the level columns are lower limits. Second, the columns in Fig. 5 are not corrected for stimulated emission, which will mainly increase the columns of the PIMS lines at long wavelengths.

2.4. Velocity shifts in Arp 220

Having confirmed the velocity calibration (or "corrections") applied to the Arp 220 spectrum (Paper I) with the second Arp 220 dataset, we now compare the line profiles and velocity shifts presented in Paper I to the velocity profiles and centroids of the molecular ions. The average profiles of several H$_2$O, OH$^+$, H$_2$O$^+$, H$_3$O$^+$, HCN and NH$_3$ lines detected in Arp 220 are compared in Fig. 6. In all panels, HE and LE

mean high-excitation and low-excitation, respectively, qualitatively indicating whether the selected lines are high-lying or low-lying lines. Thus H$_2$O HE is the average profile of two representative high-excitation lines of H$_2$O, the $6_{16} \leftarrow 5_{05}$ and $3_{22} \leftarrow 2_{11}$ lines (Paper I); H$_2$O LE is the average profile of the two low-lying $2_{12} \leftarrow 1_{01}$ and $2_{21} \leftarrow 1_{10}$ lines, and similarly for other species/excitation. The H$_3$O$^+$ PIMS spectrum is the average of the unblended high-lying, pure-inversion metastable lines of H$_3$O$^+$, and the NH$_3$ RIMS one is the average of the relatively uncontaminated rotation-inversion metastable $7_6^+ \leftarrow 6_6^-$ and $6_5^- \leftarrow 5_5^+$ lines. The averages were generating by resampling the individual spectra to a common velocity resolution, and adopting equal weights for all them. Figure 7 displays the velocity centroids of these generated line profiles.

Figures 6 and 7 indicate that there are systematic velocity shifts associated with line excitation, irrespective of the considered species. The averaged H$_2$O HE profile, peaking at
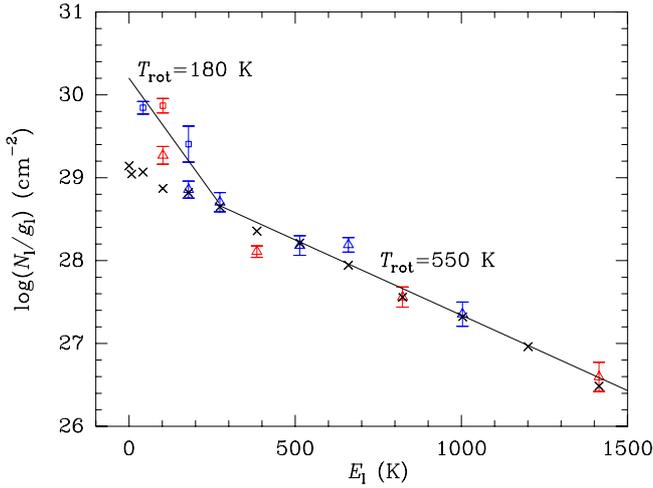
Fig. 5. Population diagram of H_3O^+ (metastable levels) in Arp 220. Red and blue symbols correspond to ortho and para levels, respectively. Columns derived from pure-inversion and rotation-inversion lines are shown with triangles and squares, respectively. The crosses indicate the expected population distribution for $T_{rot} = 550$ K and a fixed ortho-to-para ratio of 1.

-20 km s^{-1}, has a shape very similar to the averaged OH$^+$ HE (panel a), H$_2$O$^+$ HE (b), and NH$_3$ HE (d) profiles, though the latter is somewhat narrower (and relatively uncertain due to line blending). The HCN $18 \leftarrow 17$ line (panel a) could be even more blueshifted, though the signal-to-noise ratio is relatively low. On the other hand, there is a clear velocity shift in the peak absorption of the H$_2$O HE and LE averages, with the latter peaking at a velocity of $+50$ km s^{-1}. The LE averages of OH$^+$ and H$_2$O$^+$ also tend to peak at more positive velocities, though the OH$^+$ LE lines are not ground-state lines ($E_{lower} \approx 50$ K) and thus may represent an intermediate situation.

The velocity centroids of the H$_3$O$^+$ PIMS lines, however, which are characterized by high E_{lower}, peak at the velocity of the LE lines and thus present an exception to the finding discussed above. A velocity shift of ≈ 70 km s^{-1} is shown in Fig. 6c between the average H$_2$O HE and H$_3$O$^+$ PIMS spectra, with the latter peaking at the velocity of the LE lines of H$_2$O and H$_2$O$^+$. This shift is much lower than the line widths of ~ 300 km s^{-1}, but larger than our spectral calibration accuracy. The average velocity of all H$_2$O lines (excluding the lowest-lying LE lines) is -20 ± 35 km s^{-1}, whereas that of the metastable H$_3$O$^+$ lines is 50 ± 25 km s^{-1}. The latter corresponds to $v_{LSR} = 5480$ km s^{-1}, in rough agreement with the velocity centroid of the $3_2^+ - 2_2^-$ line (vdT08) and close to the central velocity of CO $2-1$ in the western nucleus (Downes & Eckart 2007). Excluding the low signal-to-noise H$_3$O$^+$ $4_1^- \leftarrow 3_1^+$ line, the other three non-metastable lines have an average velocity of 20 ± 15 km s^{-1}. The low-lying $4_3^- \leftarrow 3_3^+$ line (Fig. 4k) is even more redshifted (≈ 100 km s^{-1}), with the two data sets giving very similar line shapes. With the same lower level, the pure-inversion $3_3^- \leftarrow 3_3^+$ line (Fig. 4a) also shows hints of redshifted absorption at >100 km s^{-1}.

At the very least, the velocity shift between the peak absorption of the H$_3$O$^+$ PIMS and the HE lines of other species indicates a *spatial* shift between the regions responsible for the strongest absorption in both sets of lines. On the one hand, this may not be surprising from excitation arguments. The H$_2$O HE levels are excited through radiative pumping by dust (Paper I), and thus the corresponding lines trace the region of highest far-IR radiation density (and thus of highest T_{dust}). On

the other hand, the H$_3$O$^+$ metastable levels cannot be radiatively pumped, but are either excited through collisions indicating high T_{gas}, or reflect H$_3$O$^+$ formation in high-lying levels; thus the physical conditions that favor strong absorption in each set of lines are different and do not necessarily coincide spatially. On the other hand, the NH$_3$ RIMS lines, with $E_{lower} = 300-400$ K, are collisionally pumped but better match the H$_2$O HE profile (Fig. 6d), suggesting either chemical differences between the two velocity components, or the dominance of chemical pumping on the formation of the PIMS lines of H$_3$O$^+$.

Given the velocity coincidence between the peak absorption of the H$_3$O$^+$ PIMS lines and the H$_2$O LE lines, the question is whether the H$_3$O$^+$ PIMS lines arise from foreground gas in the direction of, but detached from the nuclear region, or the lines arise on the contrary from gas physically associated with the nuclei. The PACS spectrum of Arp 220 shows RI lines of H$_3$O$^+$ arising from non-metastable levels (Figs. 4m, l, n, p) that are radiatively pumped through dust emission. Of the above lines, the H$_3$O$^+$ $4_0^- \leftarrow 3_0^+$ at 70.8 μm is most sensitive to T_{dust}, requiring relatively high far-IR radiation densities. Figure 6h indicates a good match between the shape of the H$_3$O$^+$ 70.8 μm line and of the PIMS average, and thus it is likely that both sets of lines arise from essentially the same region. We thus expect that the H$_3$O$^+$ PIMS lines are of primarily nuclear origin though, as argued in Sect. 3.4.3, probably more extended than the region where the NH$_3$ lines are formed.

The simplest scenario that can account for the observed velocity pattern in Arp 220 consists of the H$_3$O$^+$ PIMS lines and the LE lines of other species peaking at the "rest" velocity of the western nucleus, and thus primarily tracing rotating gas together with more foreground gas, while the HE lines of H$_2$O, OH, NH$_3$, and also OH$^+$ and H$_2$O$^+$, mainly tracing an outflowing component with a line of sight velocity of ~ 75 km s^{-1}, similar to that observed in HCO$^+$ (Sakamoto et al. 2009)[5]. Besides grain mantle evaporation and neutral-neutral reactions at high T_{gas} (Paper I), sputtering in shocks could also remove the mantles and contribute to enhance the gas-phase abundances of H$_2$O and NH$_3$. Alternatively, both components may be tracing different sections of the nuclear rotating disk(s), which shows steep velocity gradients as seen in the (sub)millimeter lines of CO (Downes & Eckart 2007; Sakamoto et al. 2008).

3. Environments, column densities and abundances

3.1. The excitation of the molecular ions

Derivation of the column densities implied by the observations require calculations of excitation appropiate for the environments where OH$^+$, H$_2$O$^+$, and H$_3$O$^+$ reside. The rates for collisional excitation of these molecular ions are not known, but both Arp 220 and NGC 4418 have luminous-compact nuclear far-IR continuum sources that excite H$_2$O, OH, and other species to level energies of >500 K (Paper I). Therefore, a natural mechanism for exciting OH$^+$, H$_2$O$^+$, and the non-metastable levels of H$_3$O$^+$ along a given K-ladder is via radiatively allowed transitions through absorption of dust-emitted photons.

Collisional excitation of the high-lying lines of OH$^+$ and H$_2$O$^+$ is expected to be less efficient. The A_{ul}-Einstein coefficients are high (Table 1), and thus the critical densities (n_{cr}) are

---

[5] In Fig. 12 of Paper I, the HCO$^+$ lines should be shifted 100 km s^{-1} to the red, as the original spectrum (Sakamoto et al. 2009) uses the radio convention for the velocities; thus the HCO$^+$ absorption toward the western nucleus better matches the blueshifted absorption in the H$_2$O HE lines.
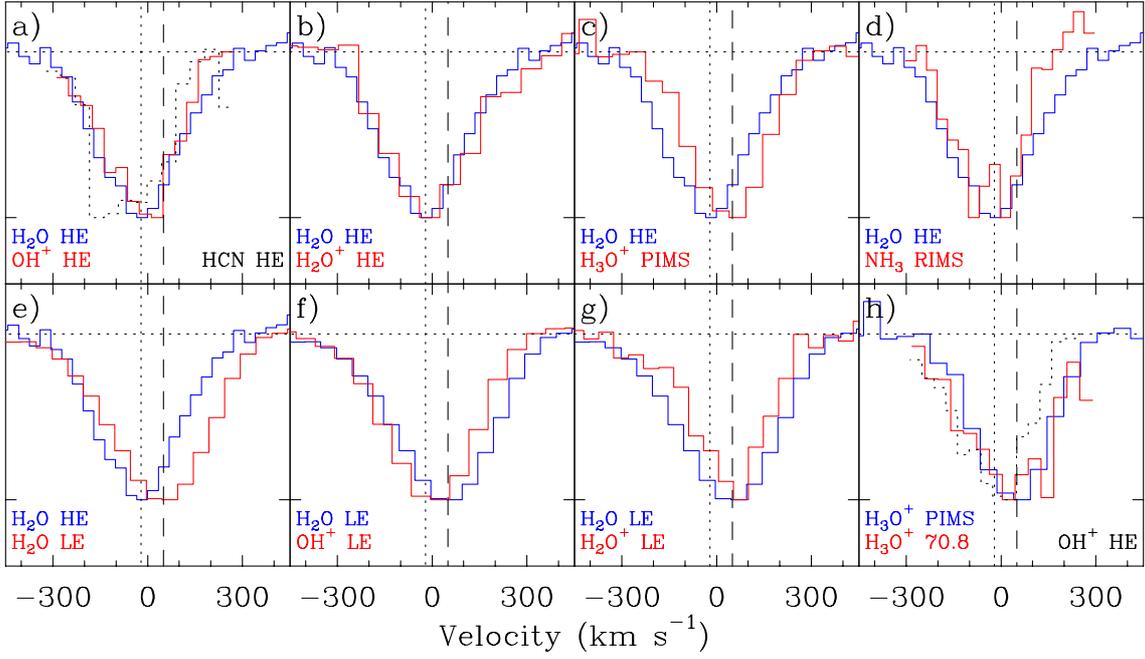
Fig. 6. Comparison between averaged line shapes of several lines in Arp 220. HE, LE, PIMS and RIMS mean high-excitation, low-excitation, pure-inversion metastable, and rotation-inversion metastable, respectively. H_2O HE is the average of the $6_{16} \leftarrow 5_{05}$ and $3_{22} \leftarrow 2_{11}$ lines of H_2O (Paper I); HCN HE is the $18-17$ line of HCN; OH^+ HE is the average of the 4_3-3_2 and 4_5-3_4 lines of OH^+; H_2O^+ HE is the average of the $3_{22} \leftarrow 2_{11}$ $7/2-5/2$, $3_{13} \leftarrow 2_{02}$ $5/2-3/2$, and $4_{04} \leftarrow 3_{13}$ $7/2-5/2$ lines of H_2O^+; H_3O^+ PIMS is the average of the pure-inversion, metastable $5_5^- - 5_5^+$, $6_6^- - 6_6^+$, $7_7^- - 7_7^+$, and $8_8^- - 8_8^+$ lines of H_3O^+; NH_3 RIMS is the average of the rotation-inversion metastable $7_6^- - 6_6^-$ and $6_5^- - 5_5^-$ lines of NH_3; H_2O LE is the average of the $2_{12} \leftarrow 1_{01}$ and $2_{21} \leftarrow 1_{10}$ lines of H_2O; OH^+ LE is the average of the 2_2-1_2, 2_1-1_0, 2_2-1_1, and 2_1-1_1 lines of OH^+; H_2O^+ LE is the average of the $2_{12} \leftarrow 1_{01}$ $5/2-3/2$ and $3/2-1/2$ lines of H_2O^+; H_3O^+ 70.8 is the $4_0^- - 3_0^+$ line of H_3O^+ at 70.8 μm. The dotted and dashed vertical lines indicate the velocity centroids of the averaged HE and LE spectra, respectively.
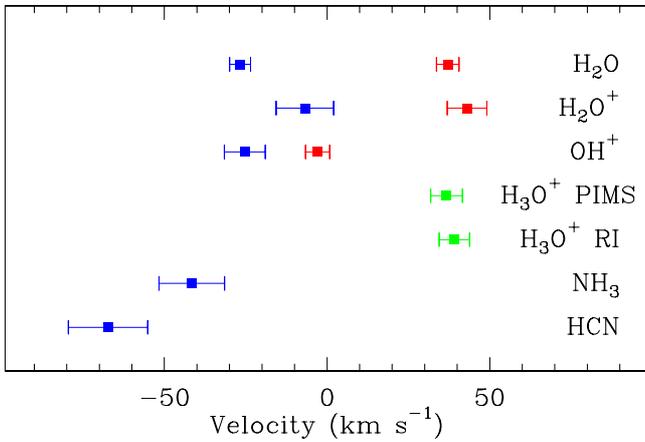
Fig. 7. Velocity centroids of the averaged line shapes in Arp 220 displayed in Fig. 6, derived from Gaussian fits. Velocities are calculated relative to $z = 0.0181$. Blue and red symbols correspond to HE and LE averages, respectively; for H_3O^+ the green symbols indicate the PIMS and RI averages. Errorbars are 1σ uncertainties.

likely to be high as well. For the $N = 1-0$ transition of OH^+, with $A_{ul} \approx 0.02$ s^{-1} and assuming a coefficient for collisional de-excitation with H and H_2 of 10^{-9} cm^3 s^{-1}, $n_{cr} \approx 2 \times 10^7$ cm^{-3}, which is much higher than the expected densities (see Sect. 4.5 below), and also higher than the nuclear densities inferred from other tracers (Paper I). As a result, the expected excitation temperature of the $N = 1-0$ transition of OH^+ from collisional excitation alone would be <20 K, in contrast with the typical values of $35-70$ K obtained from radiative excitation in the models shown below. On the other hand, excitation through collisions with electrons has rate coefficients that might be much higher

than with H and H_2, $\sim 10^{-6}$ cm^3 s^{-1} (Neufeld & Dalgarno 1989; Lim et al. 1999), and has been recently invoked by van der Tak et al. (2012) to explain the emission in the HF $1-0$ line toward the Orion Bar. However, the expected electron density is several $\times 10^3$ lower than the density of H (Fig. C.1), so that its effect on the excitation is not expected to be much higher than that of H. Finally, the detected lines are seen in absorption, and radiative pumping models generate the observed absorption features naturally, as we show below.

Another potential excitation mechanism is chemical formation in excited levels (Stäuber & Bruderer 2009), i.e. formation pumping. In environments with weak dust emission, a downward cascade after molecular formation in excited levels (e.g. Bruderer et al. 2010a) is expected to generate emission in non-metastable lines (i.e. chemoluminiscence). But again, in the specific case of NGC 4418 and Arp 220, all detected lines from molecular ions are seen in absorption, qualitatively matching the far-IR pumping scheme. Furthermore, ignoring excitation by dust emission, the equilibrium level populations of OH^+ and H_2O^+ resulting from formation pumping (see Appendix B in Bruderer et al. 2010b) yield very low excitation even for very high formation rates (see Appendix A). This is due to the very high A-Einstein coefficients (Table 1) as compared with the expected formation/destruction rates (Sect. 4). Thus we do not expect that formation pumping has a measurable effect on the excitation of non-metastable transitions in these sources.

The case of the metastable lines of H_3O^+ is different. The $K > 1$ ladders cannot be populated from $K = 0, 1$ through radiative pumping, but only through collisions or via molecular formation in high-lying levels. The latter process can be envisioned as follows: molecular formation in an excited (K, J) level will be followed by quick cascade down to the metastable $J = K$

one, where no more paths for radiative decay are available. Then, the molecule will "freeze-out" in that metastable level (ignoring here radiative excitation for simplicity) until destruction through recombination or until a collisional thermalization event takes place. If the destruction rate dominates over collisional relaxation, the observed population distribution in the metastable levels (i.e., T_{rot}) will be governed by the formation process rather than by T_{gas} (Lis et al. 2012). Writing the rate of H_3O^+ formation per unit volume as $\Gamma_{H_3O^+} = \epsilon_{H_3O^+} n_H \zeta$, where $\epsilon_{H_3O^+}$ is the efficiency with which ionizations are transfered to the production of H_3O^+ (see Neufeld et al. 2010, for OH^+), the condition for formation pumping to dominate the observed excitation over collisions can be written as[6]

$$k_{col}(T_{gas}) < 8 \times 10^{-11} \times \frac{\epsilon_{H_3O^+}}{0.4} \times \frac{\zeta/n_H}{10^{-17} \text{ cm}^3 \text{ s}^{-1}} \times \frac{5 \times 10^{-8}}{\chi(H_3O^+)}, \quad (1)$$

where k_{col} (in cm^3 s^{-1}) is the rate for collisional relaxation from a metastable level at T_{gas}, ζ is the ionization rate per H nucleus, χ denotes the abundance relative to H nuclei, and the reference value of $\epsilon_{H_3O^+} = 0.4$ is based on the chemical models of Sect. 4. Collisional rates for H_3O^+ excitation with H_2 have been calculated by Offer & van Hemert (1992)[7] for a temperature of 100 K and for the lowest H_3O^+ levels in the $K = 0, 1, 2, 3$ ladders. Taking as a guide $k_{col} \sim 2 \times 10^{-10}$ cm^3 s^{-1} at 100 K from the 3_3^+ level (Offer & van Hemert 1992), formation pumping may have important effects at high ζ/n_H, but collisional rates for higher levels and with H_2 and H are required to check this point. Calculations for excitation of H_3O^+ through electron impact (Faure & Tennyson 2003) indicate that the $\Delta K > 0$ transitions are negligible, so collisions with electrons are probably not important in populating the $K > 1$ metastable levels.

In our calculations for H_3O^+ below, we use the de-excitation rates by Offer & van Hemert (1992), and correct the excitation rates according to the value of T_{gas} in our models and the requirements of detailed balance. Since no collisional rates that connect the low- and high-K ladders are available, we simply force the metastable high-lying J_{J^+} levels to be populated according to the adopted T_{rot}, which represents T_{gas}, the signature of the formation process, or a combination of both. This will be further discussed in Sect. 5. Additionally, we attempt to establish in Appendix B under which conditions the formation process can generate the observed high excitation in environments with moderate T_{gas}. Excitation of non-metastable levels is dominated by the far-IR field, and significant discrepancies between observations and model results would indicate the relevance of alternative excitation mechanism.

3.2. Source components

As shown in Paper I, the far-IR spectra of NGC 4418 and Arp 220 cannot be described by a single set of ISM parameters, but different lines have different excitation requirements and are thus formed in different regions of the galaxies associated with different far-IR continuum components that we summarize here (see also Figs. 1 and 16 and Tables 1 and 2 in Paper I). For NGC 4418, at far-IR wavelengths we require (i) a nuclear core (C_{core}) with $T_{dust} \approx 130-150$ K, that provides absorption in the high-lying lines of H_2O, OH, HCN, and NH_3; (ii) a warm

component (C_{warm}) with $T_{dust} \approx 110-85$ K, that provides absorption in moderately excited lines of H_2O and OH as well as a significant fraction of the far-IR continuum emission; and (iii) an extended, possibly infalling component ($C_{extended}$) with $T_{dust} \approx 90-40$ K, which accounts for low-lying redshifted lines of OH and O^0. For Arp 220, we require (i) the western and eastern nuclear components (C_{west} and C_{east}), where the high-lying molecular lines are formed; (ii) the extended component ($C_{extended}$), which provides a significant fraction of the far-IR continuum emission (though mostly reemission from the nuclei) and accounts for the absorption in moderate and low-excitation lines of H_2O and OH; and (iii) an additional low-excitation, absorbing component or "halo" (C_{halo}), with no associated continuum that is required to fit the absorption in the ground-state lines of H_2O, OH, and O^0.

Calculations of excitation, line fluxes, and line profiles were first performed for the nuclear components in both sources to fit the high-lying lines, and then were done for the extended components to complete fitting of the absorption in the low-lying lines. Table 2 gives the inferred column densities, based on a "screen" approach for the nuclear components (i.e. the molecules are located in front of the nucleus) due to the high continuum opacities of these components in the far-IR; the "mixed" approach (i.e. the molecules and dust are mixed) would give columns highly exceeding the listed values (González-Alfonso et al. 2008). For the $C_{extended}$, the "mixed" approach is used owing to the much more moderate continuum opacities (Paper I).

3.3. NGC 4418

3.3.1. OH$^+$

In NGC 4418 we first used the parameters of the C_{core} and C_{warm} components as given in Paper I to match the absorption in the high-lying $4_J \leftarrow 3_{J'}$ lines of OH^+, by assuming a covering factor of 1. The OH^+ column densities were similar for both components, $N(OH^+) = (0.6-1) \times 10^{16}$ cm^{-2}, respectively. The model fits were also very similar for both components, so that we are not able to determine in which nuclear component the OH^+ lines are (primarily) formed. By using the same normalization column as in Paper I, $N(H) = 4 \times 10^{23}$ cm^{-2}, the OH^+ abundance in the nuclear region of NGC 4418 is $\chi(OH^+) = (1.5-2.5) \times 10^{-8}$. Contrary to observed, the $4_5 \leftarrow 3_4$ component in Fig. 2e is predicted to be the strongest, which could indicate significant departures of the fine-structure distribution of populations relative to the predicted one. The effective spatial extent (diameter) predicted by the C_{core} and C_{warm} models is $\approx 20-30$ pc, respectively, and $T_{dust} = 150-110$ K.

Figure 2 shows (blue curves) the model fit for the nuclear component (similar for C_{core} and C_{warm}), together with a model for NH in panel a (light-blue curve). The nuclear model that fits the $4_J \leftarrow 3_{J'}$ lines underpredicts the $2_2 \leftarrow 1_1$ line and the 153.0 μm feature (composed of the OH^+ $2_3 \leftarrow 1_2$ and the NH $2_2 \leftarrow 1_1$ lines, see Fig. 2a). The OH^+ 2_2-1_1 line has a redshifted excess, and the 153.0 μm feature cannot be fully reproduced at just the central wavelength of the feature, which is also redshifted relative to the OH^+ line. This strongly suggests that the absorption that cannot be fit with the nuclear model is due to $C_{extended}$, a more extended, inflowing component proposed in Paper I in order to explain the redshifted absorption observed in the ground-state lines of OH and [O I]. Fitting the remaining OH^+ absorption with the $C_{extended}$ model in Paper I (green curves in Fig. 2a-upper), the fit shown with the red curve in Fig. 2a

---

[6] In steady state, this condition can also be expressed as $k_{col} < 10^{-10} \times (T_{gas}/100)^{-0.5} \times (\chi(e^-)/1.4 \times 10^{-4})$ cm^3 s^{-1}, suggesting possible significant formation pumping effects in high-A_V translucent clouds (see Appendix B).

[7] Available at http://www.strw.leidenuniv.nl/~moldata/

is obtained. We infer $N(\mathrm{OH}^+) \sim 3 \times 10^{15}$ cm^{-2}, and roughly $\chi(\mathrm{OH}^+) \sim 2 \times 10^{-8}$.

In summary, the OH$^+$ lines are essentially formed in the nuclear $C_{\mathrm{warm}} + C_{\mathrm{core}}$ components, with $N(\mathrm{OH}^+) \approx (6\text{--}10) \times 10^{15}$ cm^{-2}. Some contribution to the $2_2 \leftarrow 1_1$ and $2_3 \leftarrow 1_2$ lines due to inflowing gas in C_{extended} is also inferred, with $N(\mathrm{OH}^+) \sim 3 \times 10^{15}$ cm^{-2}.

3.3.2. H$_2$O$^+$

H$_2$O$^+$ is weak in NGC 4418 (Sect. 2.2), though the $5/2 \leftarrow 3/2$ component of the $3_{22} \leftarrow 2_{11}$ transition at 89 μm, and more tentatively the $7/2 \leftarrow 5/2$ one, are detected in the source (Fig. 3d). We have carried out models for the C_{core} and C_{warm} components that fit the above lines. Both models give similar columns of $N(\mathrm{H_2O}^+) \approx 3\text{--}4 \times 10^{15}$ cm^{-2}, but fail to account for the somewhat marginal $4_{04} \leftarrow 3_{13}$ components (Fig. 3e). The C_{core} model prediction better matches these features but, as shown with blue curves in Fig. 3c, may (marginally) overestimate the $3_{13} \leftarrow 2_{02}$ components. The H$_2$O$^+$ $3_{31} \leftarrow 2_{20}$ $7/2 \leftarrow 5/2$ at 65.6 μm (panel f) is blended with NH$_2$ and ^{18}OH lines and affected by an uncertain baseline (Paper I). We conclude that the OH$^+$/H$_2$O$^+$ column density ratio in the nuclear region of NGC 4418 is in the range 1.5–2.5. The ground-state H$_2$O$^+$ lines are not detected, indicating that H$_2$O$^+$ has a low abundance in the C_{extended} component of NGC 4418.

3.3.3. H$_3$O$^+$

Only the RI lines of H$_3$O$^+$ were detected in NGC 4418. They were fitted with the C_{core} and C_{warm} components, with an assumed ortho-to-para ratio of 1. Both components give similar column densities of $N(\mathrm{H_3O}^+) \approx 5\text{--}8 \times 10^{15}$ cm^{-2}, similar to that inferred by Aalto et al. (2011) from observations of the $3_2^+ \leftarrow 2_2^-$ line. The C_{core} model is shown with blue curves in Fig. 4. The main drawback of both models is that the absorption in the $3_1^- \leftarrow 2_1^+$ transition (panel p) is significantly overpredicted; the line is not detected, possibly due to cancellation between absorption toward the continuum source and reemission from a more extended region. The OH$^+$/H$_3$O$^+$ column density ratio in the nuclear region of NGC 4418 is ≈ 1.

The PIMS lines of H$_3$O$^+$ are not detected in NGC 4418, but the model for C_{core} in Fig. 4 uses the same $T_{\mathrm{rot}} = 500$ K as in Arp 220, and the predicted faint PIMS lines are nevertheless quite compatible with the observed spectrum. The model predicts wing-like features at the wavelengths of the $9_9^- - 9_9^+$ and $12_{12}^- - 12_{12}^+$ ortho PIMS lines, which could be present in the spectrum at very low (but not significant) signal-to-noise. Therefore, the non-detection of the PIMS lines does not imply that T_{rot} is low in NGC 4418, but according to our model can also be due to moderate continuum opacity and dilution of the nuclear continuum emission at long far-IR wavelengths.

3.4. Arp 220

3.4.1. OH$^+$

In Arp 220, the high-lying OH$^+$ $4_J \leftarrow 3_{J'}$ lines shown in Fig. 2e are tentatively associated with the luminous western nucleus, C_{west}, but they can be generally interpreted as the joint emission from the two nuclei (Paper I). In our model for C_{west}, we include a velocity gradient through the absorbing shell of 130 km s^{-1}, to reproduce the observed line broadening. We use two approaches to bracket the parameters inferred in Paper I for C_{west}. For a

compact/warm region, with $T_{\mathrm{dust}} = 110$ K and $d = 93$ pc, the high-lying OH$^+$ $4_J \leftarrow 3_{J'}$ lines are well fitted with a column of $N(\mathrm{OH}^+) = 1.1 \times 10^{16}$ cm^{-2}, similar to the value found in NGC 4418. The predicted spectrum is shown with blue curves in Fig. 2. The OH$^+$ absorption in the $4_J \leftarrow 3_{J'}$ lines, however, does not require such high T_{dust}. For a colder and more extended region, with $T_{\mathrm{dust}} = 90$ K and $d = 160$ pc, the column density is $N(\mathrm{OH}^+) = 4.5 \times 10^{15}$ cm^{-2}. These models, however, do not reproduce the strong $2_J \leftarrow 1_{J'}$ and $3_2 \leftarrow 2_2$ lines (Fig. 2a–d), so another component is required in addition. We identify this additional component as C_{extended} (Paper I), which has moderate excitation in H$_2$O and OH. The C_{extended} component can be identified with the (inner region of) the external disk traced by CO (Downes & Eckart 2007). In Paper I we estimated $d \sim 650$ pc, though this is uncertain by at least a factor of 2. The additional OH$^+$ absorption could indeed be produced in a relatively small region ($d \lesssim 300$ pc) around the nuclei; our results are relatively uncertain for this component. Assuming that the extended OH$^+$ mainly absorbs the continuum of the C_{extended} component (Fig. 1 in Paper I), it most probably has a column of $N(\mathrm{OH}^+) \approx (2\text{--}4) \times 10^{16}$ cm^{-2}. This reflects the widespread presence of OH$^+$ in the regions surrounding the nuclei.

The joint contribution of C_{west} and C_{extended} to the OH$^+$ absorption, shown with a red curve in Fig. 2, yields a reasonable fit to most OH$^+$ lines in Arp 220, though the $3_2 \leftarrow 2_2$ line at 104 μm remains underpredicted (and blended with an H$_2$O line). The wing-like spectral feature at 153.45 μm is not reproduced, though it is probably due to H$_3$O$^+$ (Sect. 3.4.3).

3.4.2. H$_2$O$^+$

The above models for C_{west} were applied to H$_2$O$^+$. Using the parameters for the compact/warm approach, $T_{\mathrm{dust}} = 110$ K and $d = 93$ pc, we derive a H$_2$O$^+$ column density similar to that found for OH$^+$, $N(\mathrm{H_2O}^+) \approx 0.9 \times 10^{16}$ cm^{-2}. The model result is shown in Fig. 3 (blue curves). In this model the $3_{22} \leftarrow 2_{11}$ $5/2 \leftarrow 3/2$ and possibly the $3_{31} \leftarrow 2_{20}$ $7/2 \leftarrow 5/2$ lines are overpredicted, but the other ortho-H$_2$O$^+$ lines are well reproduced. Using the more extended, colder approach, with $T_{\mathrm{dust}} = 90$ K and $d = 160$ pc, the column density is $N(\mathrm{H_2O}^+) = 2.5 \times 10^{15}$ cm^{-2}. In the nuclear region of Arp 220, the most likely OH$^+$-to-H$_2$O$^+$ ratio is 1–2.

Apart from the para-H$_2$O$^+$ ground transition, there is only one excited, non-contaminated para-H$_2$O$^+$ line detected in the spectrum of Arp 220, the $2_{21} \leftarrow 1_{10}$ $5/2$–$3/2$ at 105.7 μm. As can be seen in Fig. 3b, the absorbing flux in this line is well reproduced with our models, which use an ortho-to-para ratio of 3, the high-temperature limit. This provides a slightly better fit than the one obtained with an ortho-to-para ratio of ≈ 4.8, the value derived by Schilke et al. (2010) toward Sgr B2, which underestimates the absorbing line flux in Arp 220 by 35%.

The ground-state p-H$_2$O$^+$ $2_{12} \leftarrow 1_{01}$ lines at 183–184 μm cannot be reproduced with the C_{west} component (Fig. 3a). Models for the C_{extended} were also unsuccessful in reproducing these spectral features, as the required high (1.6×10^{16} cm^{-2}) H$_2$O$^+$ columns have also the effect of predicting too strong absorption in other lines, specifically in the $3_{22} \leftarrow 2_{11}$ components. The p-H$_2$O$^+$ 183–184 μm lines peak at a velocity different from the H$_2$O$^+$ HE lines (Fig. 6), and are thus likely generated in a low excitation region that generates faint absorption in other lines. This component is likely to be the same as that producing strong absorption in the ground-state lines of H$_2$O and OH, i.e. the C_{halo} component (Paper I). The spatial extent of this component is not constrained, and can be interpreted as foreground gas located along the line of sight to the nuclei absorbing their

Table 2. Inferred column densities, OH$^+$ abundances, and OH$^+$/H$_2$O$^+$ and OH$^+$/H$_3$O$^+$ column density ratios.

Source	NGC 4418		Arp 220	
Component	C_{core}-C_{warm}	$C_{extended}$	C_{west}	$C_{extended}$
T_{dust} (K)	110−150	Variable^c	90−110	variable^c
N(OH$^+$)^a (10^{16} cm^{-2})	0.6−1	∼0.3	0.5−1.1	2−4
N(H$_2$O$^+$)^a (10^{16} cm^{-2})	0.3−0.4		0.25−0.9	∼0.5^d
N(H$_3$O$^+$)^a (10^{16} cm^{-2})	0.5−0.8		0.9−2.7^e	
χ(OH$^+$)^b (10^{-8})	1.5−2.5	∼ 2	1.1−2.8	∼4
OH$^+$/H$_2$O$^+$	1.5−2.5		1.0−2.0	5−10
OH$^+$/H$_3$O$^+$	∼1		∼1^e	

Notes. $^{(a)}$ Columns toward the nuclei are calculated within a screen approach. $^{(b)}$ Estimated OH$^+$ abundance relative to H nuclei, using a normalization column density of N(H) $= 4 \times 10^{23}$ cm^{-2} for the nuclear components (Paper I). $^{(c)}$ T_{dust} varies with radial position as it is calculated from the balance between heating and cooling. $^{(d)}$ The p-H$_2$O$^+$ ground-state lines at 183−184 μm in Arp 220 require an additional absorbing halo component (C_{halo}) with N(H$_2$O$^+$) ∼ $(2.5−3.0) \times 10^{15}$ cm^{-2}. $^{(e)}$ In Arp 220, the total H$_3$O$^+$ column density is twice the nuclear OH$^+$ column, but since the H$_3$O$^+$ lines are redshifted relative to the OH$^+$ lines, we roughly estimate an OH$^+$/H$_3$O$^+$ ratio of 1 in the nuclear region where the OH$^+$ lines are formed. In the $C_{extended}$ component, the OH$^+$/H$_3$O$^+$ ratio is uncertain.
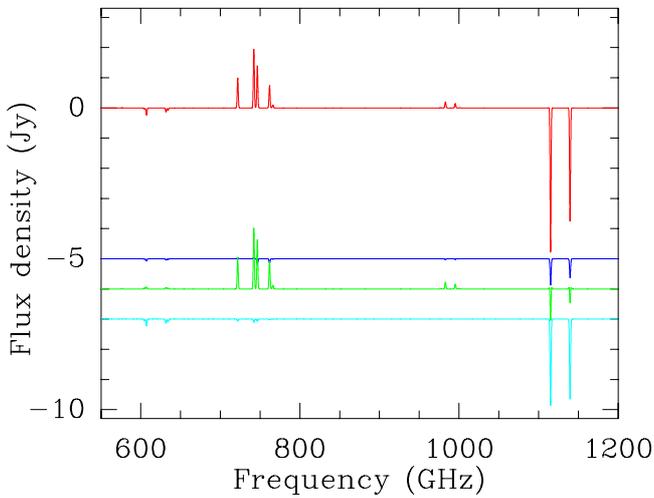
Fig. 8. Predicted SPIRE spectrum of H$_2$O$^+$ in Arp 220 between 600 and 1200 GHz. The contributions by the C_{west}, $C_{extended}$, and C_{halo} are shown with blue, green, and light-blue curves (vertically shifted for clarity), respectively, and the red curve shows the total absorption/emission.

nuclear far-IR emission. As shown below (Sect. 3.4.3), however, it probably includes gas within a few hundreds pc from the nuclei; the $C_{extended}$ and C_{halo} components are hard to separate physically[8]. The derived H$_2$O$^+$ column in this component is N(H$_2$O$^+$) ≈ 3×10^{15} cm^{-3}, and the fit is shown with a light blue curve in Fig. 3a.

The amount of H$_2$O$^+$ in $C_{extended}$ is better traced with the excited H$_2$O$^+$ detected in emission with *Herschel*/SPIRE by R11. In Fig. 8 we show the predicted SPIRE spectrum of H$_2$O$^+$ in Arp 220 between 600 and 1200 GHz. The contributions by the C_{west}, $C_{extended}$, and C_{halo} are shown with blue, green, and light-blue curves (vertically shifted for clarity), respectively, and the red curve shows the total absorption/emission. At these

frequencies, the contribution by the nuclear region (C_{west}) is not expected to be dominant. The absorption in the ground-state $1_{11} \leftarrow 0_{00}$ $J = 3/2 \leftarrow 1/2$ and $1/2 \leftarrow 1/2$ o-H$_2$O$^+$ lines at 1100−1150 GHz is expected to be dominated by the C_{halo} component, also responsible for the absorption in the ground-state p-H$_2$O$^+$ lines at 183−184 μm. Most relevant is the predicted *emission* in some H$_2$O$^+$ lines at 700−800 GHz, which are expected to arise from the $C_{extended}$ component. The strongest H$_2$O$^+$ emission lines are the $2_{02} \rightarrow 1_{11}$ $5/2 \rightarrow 3/2$ at 742.1 GHz and the $2_{11} \rightarrow 2_{02}$ $5/2 \rightarrow 5/2$ at 746.5 GHz, in agreement with the emission features reported by R11[9]. Two other transitions with significant predicted emission above the continuum are the $2_{02} \rightarrow 1_{11}$ $3/2 \rightarrow 1/2$ at 721.8 GHz and the $2_{11} \rightarrow 2_{02}$ $3/2 \rightarrow 3/2$ at 761.9 GHz. It is worth noting that the modeled emission features are generated through radiative pumping and not through collisions−collisional excitation is not included in our calculations. With a column density in $C_{extended}$ of N(H$_2$O$^+$) ≈ 5×10^{15} cm^{-2}, the lines fluxes at 700−800 GHz reported by R11 are nearly reproduced. Our models thus favor an OH$^+$/H$_2$O$^+$ column density ratio of ≳5 for $C_{extended}$, significantly higher than in the nuclear region (Table 2). In the C_{halo}, the OH$^+$/H$_2$O$^+$ is uncertain as the OH$^+$ ground-state lines are certainly saturated (R11).

3.4.3. H$_3$O$^+$

The H$_3$O$^+$ lines in Arp 220 show an intriguing behavior: on the one hand, non-metastable RI lines are detected (Figs. 4l, m, n, p); on the other hand, although they are radiatively pumped by far-IR photons to moderate excitation, these lines peak at roughly the same velocity as the LE lines of H$_2$O and H$_2$O$^+$ transitions (Fig. 6), i.e. they are redshifted relative to the HE lines of other species.

From the population diagram in Fig. 5, we have used two values for T_{rot}: 180 K up to the $K = 5$ ladder, and 500 K for higher-lying metastable levels. The blue lines in Fig. 4 show the model results with $T_{dust} = 90$ K, $d = 160$ pc, and N(H$_3$O$^+$) = 9×10^{15} cm^{-2}. The model for H$_3$O$^+$ nearly accounts for the pure-inversion metastable lines (panels a−i), which have moderate opacities ($\tau \sim 0.3−1$), though the $3_3^- \leftarrow 3_3^+$ line is slightly

---

[8] The difference between the $C_{extended}$ and C_{halo} components in our models for Arp 220 arises from radiative transfer effects. The $C_{extended}$ is characterized by optically thin, extended far-IR emission, where the molecules are still significantly excited via absorption of locally-emitted far-IR photons. The C_{halo}, however, describes foreground, low-excitation gas with strong, optically thick emission behind arising from the nuclei. The main difference may simply be the location of the molecules relative to the far-IR optically thick nuclei and the observer, thus basically describing the same spatially extended gas.
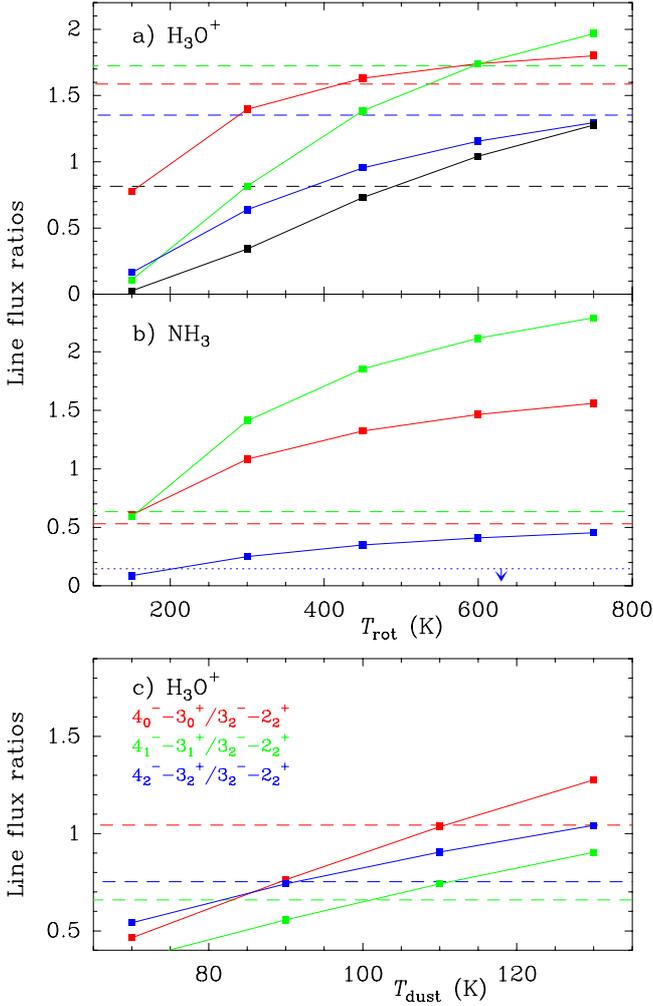
[9] R11 assigned the 746.5 GHz feature to the $2_{02} \rightarrow 1_{11}$ $3/2 \rightarrow 3/2$ at nearly the same frequency, but this transition has an Einstein coefficient 5.4 lower than the main $5/2 \rightarrow 3/2$ component and is expected to give weak emission.

Fig. 9. Model results for H$_3$O$^+$ and NH$_3$ in Arp 220. **a)** Ratios of pure inversion metastable lines of H$_3$O$^+$ versus $T_{\rm rot}$: $K = 6/K = 4$ (red), $K = 8/K = 4$ (blue), $K = 9/K = 4$ (green), and $K = 10/K = 4$ (black). **b)** For NH$_3$, the fluxes of the $6_5^- - 5_5^+$ (red), $7_6^+ - 6_6^-$ (green), and $8_6^- - 7_6^+$ (blue) are normalized to the flux of the 124.9 μm feature (composed of the $4_0 - 3_0$ and $4_1^- - 3_1^+$ NH$_3$ lines, Paper I). **c)** Ratios of rotation-inversion lines of H$_3$O$^+$ as a function of $T_{\rm dust}$. Dashed lines in all panels indicate the measured values, with typical uncertainties of 20%.

underpredicted. The rotation-inversion lines (panels j−p) are more optically thin.

Figure 9a shows the flux ratios of the pure inversion, metastable $6_6^- \leftarrow 6_6^+$, $8_8^- \leftarrow 8_8^+$, $9_9^- \leftarrow 9_9^+$, and $10_{10}^- \leftarrow 10_{10}^+$ lines to the $4_4^- \leftarrow 4_4^+$ line (solid lines) as a function of $T_{\rm rot}$, and compares them with the measured values (dashed lines). The flux measured for the $9_9^- \leftarrow 9_9^+$ line has been estimated from the total flux of the broad 165.8 μm feature by subtracting the modeled contribution due to NH$_3$ (Fig. 4g). The $K = 8/K = 4$ (blue) and $K = 9/K = 4$ (green) ratios indicate $T_{\rm rot} \sim 600-800$ K, while the $K = 6/K = 4$ (red) and $K = 10/K = 4$ (black) favor ~ 450 K. The high $T_{\rm rot}$ inferred from the H$_3$O$^+$ lines is in striking contrast with that inferred from NH$_3$ (Fig. 9b): the NH$_3$ line ratios indicate $T_{\rm rot} \sim 150$ K, in general agreement with the value inferred by Ott et al. (2011) from the pure inversion lines, and with the HCN excitation (Paper I). Either the two species are sampling different regions, and/or $T_{\rm rot}$ as derived from H$_3$O$^+$ better reflects the formation process rather than $T_{\rm gas}$.

The strength of the non-metastable rotation-inversion lines is sensitive to $T_{\rm dust}$, and in Fig. 9c we compare the fluxes of some

of these lines relative to that of the metastable $3_2^- \leftarrow 2_2^+$ line. We focus in this analysis on those lines that have similar line shapes, i.e. the $4_0^- \leftarrow 3_0^+$, $4_1^- \leftarrow 3_1^+$, and $4_2^- \leftarrow 3_2^+$ transitions. Comparison with the measured values favors $T_{\rm dust} \sim 90-110$ K. The most reliable comparison is between the $4_2^- \leftarrow 3_2^+$ and the $3_2^- \leftarrow 2_2^+$, as they belong to the same K-ladder, favoring $T_{\rm dust} \sim 90$ K. Furthermore, due to the warmer SED, $T_{\rm dust} = 110$ K generally underestimates the PIMS lines relative to the RI lines. In contrast, the H$_2$O HE lines are compatible with higher $T_{\rm dust}$ (Paper I), and detection of the NH$_3$ $6_0^- \leftarrow 5_0^+$ and $6_1^- \leftarrow 5_1^+$ lines at 83.85 μm (Paper I and confirmed with the new data set), with $E_{\rm low} \sim 400$ K and pumped through radiation, better supports $T_{\rm dust} = 110-130$ K for NH$_3$.

The value of $N($H$_3$O$^+)$ depends on the size of the far-IR continuum source. To produce the observed H$_3$O$^+$ absorptions, the models strongly favor optically thick far-IR continuum emission up to at least 180 μm. An upper limit to the size would then be 230 pc, as the continuum source with $T_{\rm dust} = 90$ K would produce the entire bolometric luminosity of the galaxy, 1.5×10^{12} $L_\odot$. This upper limit is, however, unreliable, as $C_{\rm extended}$ is expected to generate some far-IR emission, and there is also an important fraction of the luminosity associated with dust warmer than 90 K. Sizes smaller than 100 pc are also unlikely, as the H$_3$O$^+$ PIMS lines would become optically thick, and the fit to the whole H$_3$O$^+$ SLED would get worse (specifically the $6_6^- \leftarrow 6_6^+$ line would be underpredicted due to saturation). We estimate $d = 105-160$ pc, overlapping with, but at the high end of our derived size range for the nuclear OH$^+$ and H$_2$O$^+$ (93−160 pc) and significantly smaller than our estimate for the extended region as derived from the continuum emission ($\sim$650 pc, Paper I). This size range implies a column density range of $N($H$_3$O$^+) = (2.7-0.9) \times 10^{16}$ cm^{-2}. These columns are a factor of 2 higher than those of OH$^+$ for the same source sizes. However, the H$_3$O$^+$ transitions do not have the same line shapes as the OH$^+$ lines (Fig. 6h). There is, nevertheless, a good match between the OH$^+$ HE and H$_3$O$^+$ 70.8 μm profiles on the blueshifted side, suggesting some spatial overlap between both components. On these grounds, we favor a column density ratio OH$^+$/H$_3$O$^+$ ~ 1 in the nuclear region of Arp 220, with an uncertainty of ± 50%. The relatively large size found for the H$_3$O$^+$ absorption, the shift of the peak of the H$_3$O$^+$ velocity profile towards those of the low excitation lines, and the moderate $T_{\rm dust}$ found for the H$_3$O$^+$ lines, suggest that the H$_3$O$^+$ lines, while nuclear, trace a transition region between the high-excitation (HE) component and the extended component.

The model in Fig. 4 predicts a flux for the $3_2^+ \rightarrow 2_2^-$ 365 GHz line of 1.1×10^{-23} W cm^{-2}, a factor of 1.5 lower than measured by vdT08. The modeled line is slightly inverted but with negligible amplification, and thus behaves as optically thin with the flux proportional to the column. Either it is sampling in addition deep regions that are extincted in the far-IR, or it is sampling a larger region (vdT08), because the 365 GHz emission line does not require far-IR optically thick continuum emission behind.

3.5. Summary

The analysis of the O-bearing molecular ions in NGC 4418 and Arp 220 reveal (i) high nuclear OH$^+$ column densities of $(0.5-1) \times 10^{16}$ cm^{-2} in both sources, with estimated abundances relative to H nuclei of $(1-3) \times 10^{-8}$; (ii) OH$^+$/H$_2$O$^+$ column density ratios of $\sim 1-2.5$, with NGC 4418 at the high end of the range; (iii) high OH$^+$ columns of $\sim (2.5-4) \times 10^{16}$ cm^{-2} in the $C_{\rm extended}$ component of Arp 220, with an estimated abundance

of $\sim 4 \times 10^{-8}$, as well as a high OH^+/H_2O^+ ratio of $\sim 5-10$; (iv) H_3O^+ column densities of $\sim (0.5-0.8) \times 10^{16}$ cm^{-2} in NGC 4418 and $\sim (0.9-2.7) \times 10^{16}$ cm^{-2} in Arp 220, the latter essentially nuclear but likely tracing a region slightly more extended than that traced by OH^+. In the nuclear region where the OH^+ lines are formed, $OH^+/H_3O^+ \sim 1$ is estimated.

4. Chemistry

4.1. Framework

The O-bearing molecular ions are expected to be formed in gas irradiated by cosmic rays or X-rays (Maloney et al. 1996; Gerin et al. 2010; Neufeld et al. 2010; Meijerink et al. 2011). The sequence is initiated by the ionization of H atoms and H_2 molecules; OH^+ and H_2O^+ are subsequently produced by ion-neutral chemistry, and their abundances are sensitive to the gas ionization rate ζ and the molecular fraction f_{H_2}. In regions with a significant atomic fraction, H^+ transfers its charge to atomic oxygen, and the O^+ reacts with H_2 to form OH^+; H_2O^+ is then formed from $OH^+ + H_2$, and similarly H_3O^+ from $H_2O^+ + H_2$ (Gerin et al. 2010; Neufeld et al. 2010). In regions with high molecular fraction, OH^+ and H_2O^+ can also be formed via $H_3^+ + O$ (e.g. Herbst & Klemperer 1973; Gerin et al. 2010; Hollenbach et al. 2012). Furthermore, in environments with high reservoirs of OH and H_2O, OH^+ and H_2O^+ can be produced from the charge exchange reactions $OH + H^+$ and $H_2O + H^+$, as well as from photoionization of OH and H_2O (Gupta et al. 2010), while H_3O^+ may also be formed from $H_2O + H_3^+$. Finally, H^+ can also be produced through $C^+ + OH$ and $CO^+ + H$, and this FUV/chemical route does not require X/cosmic ray irradiation (Sternberg & Dalgarno 1995; Hollenbach et al. 2012).

In order to discriminate between the above paths of OH^+, H_2O^+, and H_3O^+ production, and to infer the physical conditions implied by the observations, we have run a grid of chemical models with the code described by Bruderer et al. (2009), based on previous works by Stäuber et al. (2005) and Doty et al. (2002). The chemical models calculate the steady state abundances of all relevant species based on the UMIST06 reaction rates (Woodall et al. 2007). In our simple models, the gas with H nuclei density n_H and molecular fraction f_{H_2} is directly exposed to a cosmic ray and/or X-ray flux that produces a total ionization rate per H nucleus ζ (including secondary ionizations). We ignore any other external agent (e.g. dissociating UV radiation) in the calculations, though internally generated UV radiation is included.

In their models for the production of the O-bearing molecular ions in interstellar clouds, Hollenbach et al. (2012) found that PAHs have important effects on their expected abundances. Specifically, a fraction of H^+ ions produced by cosmic rays was found to be neutralized mostly by PAH$^-$, truncating the path for the production of OH^+, and thus reducing the efficiency ϵ_{OH^+} of OH^+ formation relative to previous calculations (Neufeld et al. 2010). Recent observations of both OH^+ and H_3^+ toward the Galactic W51 by Indriolo et al. (2012) have indeed indicated a relatively low value of ϵ_{OH^+}. In NGC 4418, however, PAH emission is very weak (Spoon et al. 2007), and it is also weak in Arp 220 relative to the submillimeter continuum (Haas et al. 2001). Although this may be due to extinction of nuclear far-UV photons or foreground mid-IR extinction, rather than low PAH abundance, we conservatively switch-off the charge exchange between gas and dust grains in our calculations. In this respect, the ionization rate ζ we derive below (Sect. 4.5) should be viewed as a lower limit.
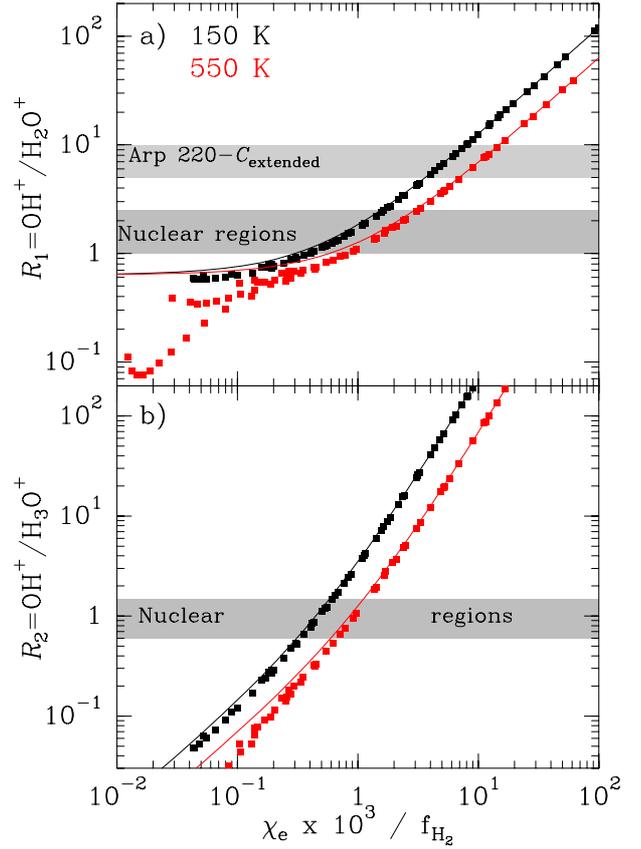
Fig. 10. Predicted **a)** OH^+/H_2O^+ and **b)** OH^+/H_3O^+ ratios as a function of $\chi_e \times 10^3/f_{H_2}$. Symbols show results for all generated chemical models, while the solid lines show the analytic curves by Gerin et al. (2010) and Neufeld et al. (2010). The inferred OH^+/H_2O^+ ratios in the nuclear regions of NGC 4418 and Arp 220, and in the $C_{extended}$ of Arp 220, are indicated with the shaded dark and light regions, respectively. Gas temperatures of 150 K (black) and 550 K (red) are assumed.

Under our simplified assumptions, and as shown by previous studies (e.g. Maloney et al. 1996; Neufeld et al. 2010; Hollenbach et al. 2012), the relevant input parameters are ζ/n_H, f_{H_2}, the gas temperature (T_{gas}), and the oxygen abundance in the gas phase (χ_O). For the latter parameters we adopt $T_{gas} = 150$ and 550 K, and solar metallicities with $\chi_O = 3 \times 10^{-4}$. Freeze-out of atomic oxygen on grains surfaces is thus ignored owing to the high T_{dust} in the nuclear regions of these sources (e.g. Hollenbach et al. 2012).

In the calculations, we treat f_{H_2} as an independent parameter, even though its value can in principle be obtained from the H_2 formation and destruction rates. Treating f_{H_2} as a free parameter has the advantage that it allows us to run simple single-point models without additional assumptions on the geometry or H_2 formation efficiencies. Furthermore, f_{H_2} also depends on other physical processes that are difficult to evaluate in the sources under study: photodissociation by UV radiation, and the evolutionary state of the cloud in low density (diffuse) clouds, where f_{H_2} only attains steady state after $\gtrsim 10$ Myr (Liszt 2007). Concerning the latter point, the ground-state lines of OH^+ and H_2O^+ have been detected in Galactic diffuse clouds indicating a very low f_{H_2} (Gerin et al. 2010; Neufeld et al. 2010), probably reflecting regions that are evolving in f_{H_2}. Our calculations are intended to describe the observations of both the nuclear regions and the extended component in Arp 220; in the latter case similar conditions to those found in Galactic diffuse clouds may

be present. For a given ζ/n_H, the maximum value that f_{H_2} can attain is described as[10]:

$$f_{H_2}^{max} = \left(1 + \frac{\zeta/n_H}{\gamma_{H_2}}\right)^{-1} = \left(1 + \frac{\zeta/n_H}{3.7 \times 10^{-17} \, cm^3 \, s^{-1}}\right)^{-1}, \qquad (2)$$

where we have adopted for the rate coefficient of H$_2$ formation on grain surfaces the reference value $\gamma_{H_2} = R_G T_g^{1/2}$ with $R_G = 3 \times 10^{-18}$ cm^3 s^{-1} and $T_{gas} = 150$ K, and applied this constant value to all cases (i.e. regardless of T_{gas} and T_{dust}) for simplicity (see discussion in Kaufman et al. 1999). For the ζ/n_H values considered in the following sections, 5×10^{-19}, 5×10^{-18}, 2×10^{-17}, 5×10^{-17}, and 5×10^{-16} cm^3 s^{-1}, $f_{H_2}^{max}$ is estimated as 0.99, 0.88, 0.65, 0.43, and 0.07, respectively. Values of f_{H_2} below $f_{H_2}^{max}$ are obtained in our models by manually increasing the H$_2$ destruction rate. Equation (2) appears to be roughly consistent with the models by Bayet et al. (2011), who obtain $f_{H_2} \approx 0.7$ at high A_V for $\zeta/n_H = 10^{-17}$ cm^3 s^{-1} and solar metallicities. However, the actual $f_{H_2}^{max}$ values could be lower, owing to the decreasing H$_2$ recombination efficiency in warm grains ($\gtrsim$100 K; Cazaux & Tielens 2004; Cuppen et al. 2010). The grid of models cover the $\zeta/n_H - f_{H_2}$ plane, with f_{H_2} varying from 0.02 to $f_{H_2}^{max}$, and ζ/n_H up to 5×10^{-16} cm^3 s^{-1}.

4.2. The OH$^+$/H$_2$O$^+$ and OH$^+$/H$_3$O$^+$ ratios

Figure 10 shows with squares, for all generated models, the predicted $R_1 \equiv$ OH$^+$/H$_2$O$^+$ and $R_2 \equiv$ OH$^+$/H$_3$O$^+$ ratios as a function of $\chi_e \times 10^3/f_{H_2}$, where χ_e is the electron abundance relative to H nuclei. As shown by Gerin et al. (2010) and Neufeld et al. (2010), if the H$_2$O$^+$ is exclusively formed by reaction of OH$^+$ with H$_2$, R_1 only depends on χ_e/f_{H_2} and T_{gas}, regardless of the formation mechanism of OH$^+$, according to:

$$R_1 \equiv OH^+/H_2O^+ = 0.63 + 0.85 \times \frac{\chi_e \times 10^3}{\sqrt{T_{300}} f_{H_2}}, \qquad (3)$$

where $T_{300} = T_{gas}/300$ K. If in addition H$_3$O$^+$ is exclusively formed from H$_2$O$^+$ + H$_2$, R_2 is given by

$$R_2 \equiv OH^+/H_3O^+ = 0.86 \times \frac{\chi_e \times 10^3}{\sqrt{T_{300}} f_{H_2}} \times \left(1 + 1.34 \times \frac{\chi_e \times 10^3}{\sqrt{T_{300}} f_{H_2}}\right). \qquad (4)$$

These analytical dependences are shown with solid curves for $T_{gas} = 150$ and 550 K in Fig. 10. Equation (3) shows that a lower limit of $R = 0.63$ is expected when recombination of H$_2$O$^+$ is ignorable and the unique route of H$_2$O$^+$ destruction is reaction with H$_2$ yielding H$_3$O$^+$. For $\chi_e/f_{H_2} \gtrsim 10^{-3}$, recombination of H$_2O^+$ becomes increasingly important and R_1 rises linearly with χ_e/f_{H_2}. This analytic approach to R_1 is appropriate for regions where the formation of H$_2$O$^+$ is dominated by H$_2$ + OH$^+$. However, at low χ_e/f_{H_2} values, i.e. in shielded/high density regions with low electron fraction and high molecular fraction, R_1 deviates from the analytic curve because there are competing paths for H$_2$O$^+$ formation (mostly H$^+$ + H$_2$O and H$_3^+$ + O) that do not involve formation of OH$^+$, thus decreasing the OH$^+$/H$_2$O$^+$ ratio below 0.63 (squares in Fig. 10a). On the other hand, R_2 varies strongly with χ_e/f_{H_2}, and significant

departures from the analytical approach in Eq. (4) are also obtained for low χ_e/f_{H_2}, and high T_{gas}.

Even in the nuclear regions of NGC 4418 and Arp 220 where densities are high and high concentration of molecular species are observed (Paper I), we do find relatively high values of R_1 and R_2, though significantly lower than in Galactic diffuse clouds. R_1 is found $\sim 1-2$ and could be even higher in NGC 4418, and $R_2 \sim 1$ (Table 2). Thus the inferred ratios appear to indicate that the primary route for H$_2$O$^+$ and H$_3$O$^+$ formation in the nuclear regions of NGC 4418 and Arp 220 is the same as in Galactic translucent clouds, H$_2$ + OH$^+$ and H$_2$ + H$_2$O$^+$, respectively, additional routes for H$_2$O$^+$ and H$_3$O$^+$ formation being less important. We still expect, however, f_{H_2} to be significantly higher than in translucent clouds. Adopting conservatively $f_{H_2} \gtrsim 0.5$, we obtain $\chi_e \gtrsim 2 \times 10^{-4}$. This value is higher than that expected from complete ionization of carbon, 1.4×10^{-4}, pointing to a significant, additional source of free electrons arising from H and H$_2$ ionization. In the more extended and diffuse $C_{extended}$ of Arp 220, the high value of R_1 probably reflects a relatively low value of f_{H_2}, resembling the situation found in Galactic translucent clouds.

The full chemical results for OH$^+$, H$_2$O$^+$, and H$_3$O$^+$, together with the corresponding abundances of electrons and H$^+$, are shown in Appendix C, where some analytical approaches to the abundance of OH$^+$ are also derived. We find that the most likely path for OH$^+$ formation is O$^+$ + H$_2$, with the contribution from the charge exchange reaction H$^+$ + OH and from direct OH ionization being of secondary importance even in the nuclear regions, where high OH abundances are inferred (Paper I). Therefore, the sequence H$^+$ $\rightarrow$ O$^+$ $\rightarrow$ OH$^+$ $\rightarrow$ H$_2$O$^+$ $\rightarrow$ H$_3$O$^+$ is favored as the production of the O-bearing cations. In Appendix C we also favor deep penetration of X-cosmic rays as the main source of H$^+$ production, with the contribution due to the C$^+$ + OH $\rightarrow$ CO$^+$ + H $\rightarrow$ CO + H$^+$ FUV/chemical route (Sternberg & Dalgarno 1995; Hollenbach et al. 2012) being presumably important only in small volumes around O stars.

4.3. The value of ζ/n_H in the extended region of Arp 220

In the $C_{extended}$ component of Arp 220, where high OH$^+$ column and R_1 values are found, our best fit values for ζ/n_H and f_{H_2} are $(0.5-2) \times 10^{-17}$ cm^3 s^{-1} and $0.05-0.25$, respectively (Fig. C.1). With this low molecular fraction, however, χ_{OH^+} is not far from saturation (see Appendix C), which occurs at $\chi_{OH^+} \gtrsim 10^{-7}$ and thus may be reached in some regions of $C_{extended}$. The low value of f_{H_2} indicates that either the H$_2$ abundance has not fully evolved to steady state, or H$_2$ photodissociation keeps a large hydrogen fraction in atomic form. The electron abundance is expected to be in the range $\chi_e \sim (3-10) \times 10^{-4}$.

These physical conditions are derived from the apparently high OH$^+$ column in $C_{extended}$, and from the relatively low H$_2$O$^+$ column with the following caveat. The columns are derived from far-IR OH$^+$ absorption and submillimeter H$_2$O$^+$ emission lines, which may probe different regions. The lowest-lying absorption lines of H$_2$O$^+$ at $183-184$ μm, observed in absorption toward the nuclei (C_{halo}), indicate a foreground H$_2$O$^+$ column of $\sim 3 \times 10^{15}$ cm^{-2}. A fraction of the H$_3$O$^+$ observed toward the nuclei is expected to arise also from foreground gas, with a column of also several $\times 10^{15}$ cm^{-2}, though detailed models for PDRs irradiated by cosmic rays show that H$_3$O$^+$ attains significant columns deeper into the cloud than OH$^+$ (Hollenbach et al. 2012). The extended gas in Arp 220 likely harbors regions with a diversity of physical conditions.

---

[10] It is assumed that each H$_2$ ionization gives rise to one net H$_2$ destruction due to the expected dominant paths H$_2^+$ + H$_2$ $\rightarrow$ H$_3^+$ + H and H$_3^+$ + e $\rightarrow$ H$_2$ + H.
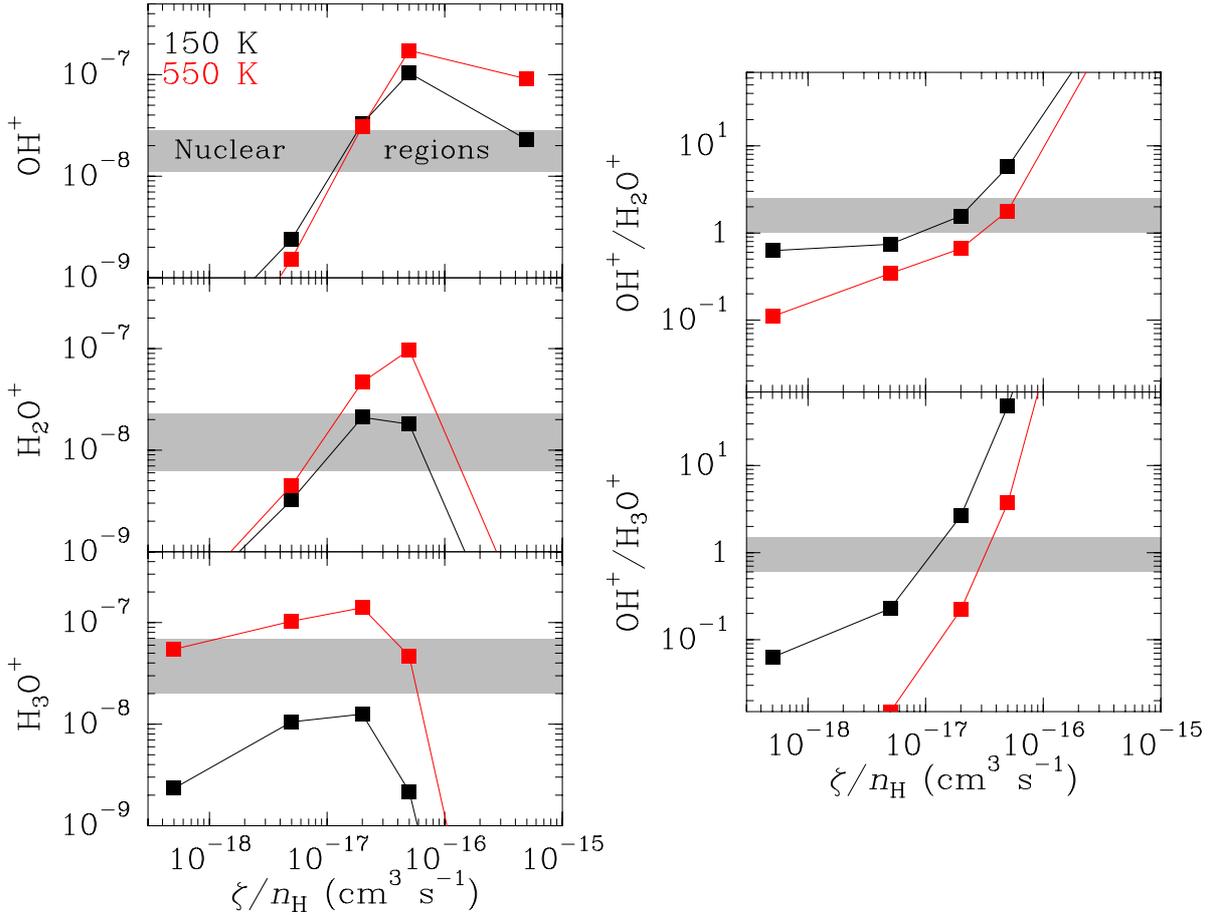
Fig. 11. Predicted OH^+, H_2O^+, and H_3O^+ abundances (*left panels*) and OH^+/H_2O^+ and OH^+/H_3O^+ abundance ratios (*right panels*) as a function of ζ/n_H. In all these models, the molecular fraction is given by the maximum value $f_{H_2}^{max}$ in Eq. (2). Gas temperatures of 150 K (black) and 550 K (red) are assumed. The ranges derived from the observations and models for the nuclear regions of NGC 4418 and Arp 220 are indicated by the shaded regions.

4.4. The value of ζ/n_H in the nuclear regions

In the nuclear regions of NGC 4418 and Arp 220, where $\chi_{OH^+} \sim 2 \times 10^{-8}$ and $R_1 = 1-2.5$ (Table 2), χ_{OH^+} is unsaturated (see Appendix C), i.e. results are sensitive to ζ/n_H. However, the inferred ζ/n_H depends on the assumed f_{H_2}. In these regions, we may expect steady state for H_2, and we adopt f_{H_2} as given by Eq. (2) (i.e. we assume that cosmic/X rays are the only source of gas dissociation/ionization). Figure 11 shows the corresponding modeled cation abundances and ratios. Model results can be summarized as follows (see also Neufeld et al. 2010; Gerin et al. 2010; Gupta et al. 2010; Hollenbach et al. 2012). For very high ζ/n_H, OH^+ can still attain high abundances even with low $f_{H_2} < 10\%$, but H_2O^+ is primarily destroyed through recombination and the abundances of H_2O^+ and H_3O^+ are low. For low ζ/n_H, low abundances of OH^+ and H_2O^+ are obtained, but the H_3O^+ abundance for $T_{gas} = 550$ K remains high as H_3O^+ is formed through reaction of highly abundant H_2O with H_3^+ and H^+. Abundances of OH^+ and H_2O^+ around 10^{-8} are obtained at typical $\zeta/n_H \sim 10^{-17}$ cm^3 s^{-1}. The abundance of H_3O^+ is very sensitive to T_{gas}, and R_2 is very sensitive to both T_{gas} and ζ/n_H.

The inferred abundances and ratios, marked by shaded regions in Fig. 11, are consistent with ζ/n_H in the range $(1-2) \times 10^{-17}$ cm^3 s^{-1}. The electron abundance is expected to be in the range $\chi_e \sim (1.5-5) \times 10^{-4}$. These results are sensitive to the assumed H_2 fraction, with higher (lower) f_{H_2} implying higher (lower) ζ/n_H. Decreasing γ_{H_2} in Eq. (2) to 10^{-17} cm^3 s^{-1}, the observed abundances and ratios can be explained with $\zeta/n_H \sim 5 \times 10^{-18}$ cm^3 s^{-1}. Further study of the H_2 reformation on warm dust grains in these regions is required to refine our estimates.

4.5. The total ionization rate per H nucleus (ζ)

Estimation of the total ionization rate per H nucleus ζ requires knowledge of the gas density. In the $C_{extended}$ of Arp 220, an average density of $n_H \sim 10^3$ cm^{-3} is expected from the continuum emission and estimated size (Paper I). Therefore $\zeta \sim 10^{-14}$ s^{-1}, about 100 times higher than in Galactic diffuse clouds. This value is however uncertain, as the absorption in the OH^+ lines may be selectively produced in regions with densities much lower than the estimated average, and thus ζ significantly lower than our above estimate is not ruled out.

In the nuclear regions of NGC 4418 and Arp 220, very high densities are expected. In the C_{core} of NGC 4418, densities of 3×10^6 cm^{-3} are derived from the faint OH absorption in the ground-state lines at central velocities, from the pattern of H_2O absorption, and from the high excitation of HCN (Paper I). If the observed OH^+ were formed in this region, this would imply an extreme, very unlikely value of $\zeta \sim 10^{-10}$ s^{-1}. However, it is plausible that the OH^+ lines are formed in a more

tenuous, nuclear region. There are several observations indicating that the molecular ions are formed in a component different from that responsible for the emission/absorption observed in neutral molecular species. Gupta et al. (2010) have detected broad blueshifted absorption in the ground-state lines of OH$^+$ and H$_2$O$^+$ with HIFI toward the Orion KL, and their preliminary models appear to point toward a component of the low-velocity Orion outflow that has a density ($\sim 10^3$ cm^{-3}) far below the densities inferred from other species. In diffuse gas, Neufeld et al. (2010) show that the velocity distribution of the OH$^+$ and H$_2$O$^+$ absorption is dissimilar from that of H$_2$O; the absorption in the molecular ions (and atomic H) being more broadly distributed in velocity space. Theoretically, the models by Bayet et al. (2011) and Meijerink et al. (2011) indicate that the OH$^+$ abundance is anticorrelated with the abundance of NH$_3$ and HCN. Furthermore, the models by Meijerink et al. (2011) indicate that the H$_2$O abundance is anticorrelated with ζ/n_{H}, and thus with the abundances of OH$^+$ and H$_2$O$^+$ as well.

We thus conservatively propose that the absorption observed in the high-lying lines of OH$^+$ and H$_2$O$^+$ are formed in a relatively low-density region different from the dense component that accounts for the absorption in the high-lying lines of H$_2$O, HCN, and NH$_3$ (Paper I). This low density component could be interpreted in terms of a nuclear interclump medium, or a shell surrounding the high density nuclear gas. However, this component cannot be very extended as otherwise the far-IR radiation density could not excite the molecular ions up to the observed rotational levels ($E_{\mathrm{lower}} \approx 285$ K). The width of the OH$^+$ shell should be small in comparison with the radius of the far-IR source, which provides a lower limit on the density. Our models favor densities of at least $\sim 10^4$ cm^{-3} in Arp 220, and $\sim 2 \times 10^4$ cm^{-3} in NGC 4418. For a density threshold of 10^4 cm^{-3}, $\zeta \gtrsim (1-2) \times 10^{-13}$ s^{-1}. In NGC 4418, where high densities were inferred in Paper I, this is a strong lower limit, and yet still $\zeta \gtrsim$ several $\times 10^2$ times the highest values currently estimated in the Milky Way (several $\times 10^{-16}$ s^{-1}; e.g. Indriolo et al. 2007, 2012; Neufeld et al. 2010; Hollenbach et al. 2012).

5. Discussion

5.1. The O-bearing cations and the neutral species

Under the simple assumptions used in our schematic chemical models, predictions for the abundances of the neutral species OH, H$_2$O, NH$_3$, and HCN analyzed in Paper I are also obtained. The main results for the neutral species are: (i) OH attains abundances $>10^{-6}$ even for the lowest $\zeta/n_{\mathrm{H}} = 5 \times 10^{-19}$ cm^3 s^{-1} and a wide range in f_{H_2}, in rough agreement with the derived values. (ii) H$_2$O only attains the inferred high abundances of $\sim 10^{-5}$ for high T_{gas} and $\zeta/n_{\mathrm{H}} < 2 \times 10^{-17}$ cm^3 s^{-1}; otherwise gas-grain chemistry (not included in our simple chemical calculations) is required to account for the high H$_2$O abundance (Paper I). (iii) HCN only approaches abundances as high as $\sim 10^{-6}$ for the lowest $\zeta/n_{\mathrm{H}} = 5 \times 10^{-19}$ cm^3 s^{-1} and high T_{gas}, suggesting that indeed it is formed in regions with densities higher, and probably more protected from the ionization source, than those responsible for the molecular ions. (iv) NH$_3$ attains abundances of only 10^{-8}, far below the inferred ones, further indicating the importance of gas-grain chemistry. In general, clumpy regions with high contrast in n_{H}, f_{H_2}, and ζ, and gas-grain chemistry, are most likely required to account for the full molecular absorption detected in the nuclear regions of both galaxies. The neutral/ion connection will be further analyzed in a future study.

5.2. X-rays or cosmic rays?

In the starburst galaxies NGC 253 and M82, detection of γ-rays (Acero et al. 2009; Acciari et al. 2009; Abdo et al. 2010) indicate a high CR energy density of $\sim 200-300$ times the value (~ 1 eV/cm^3) in the Milky Way (Abramowski et al. 2012; Persic & Rephaeli 2012). Since the γ-rays are thought to be the result of cosmic rays accelerated by supernova remnant shocks that interact with high density target material, a high rate of cosmic-ray ionization indicates a high rate of supernovae in the central region of starburst galaxies ($\nu_{\mathrm{SN}} \sim 0.03$ yr^{-1} in NGC 253, Engelbracht et al. 1998), which would be expected to be accompanied by observable galactic outflows. These are indeed seen in both NGC 253 and M82 (e.g. Sugai et al. 2003; Strickland & Heckman 2007; Veilleux et al. 2009).

The cosmic-ray energy density inferred in Arp 220 from both the supernova rate (~ 4 yr^{-1}, Lonsdale et al. 2006) and synchrotron radio emission is $\sim 500-1000$ times the Galactic value (Persic & Rephaeli 2012), in good agreement with our lower limit of several $\times 10^2$ times the Galactic value for ζ. The blueshifted component in Arp 220 traced by the high-excitation lines of H$_2$O, OH, NH$_3$, and HCN may indicate outflowing gas with a line of sight velocity of ~ 75 km s^{-1} (Sect. 2.4). With an extent of ~ 80 pc, this would imply a (local) very high mass outflow rate of $\sim 900 \times (n_{\mathrm{H}}/10^5$ cm$^{-3}) M_\odot$ yr^{-1}. However, the outflowing gas is difficult to distinguish from the rotating gas for the relatively low outflow velocities in Arp 220 (Sect. 2.4), in stark contrast with the ~ 1000 km s^{-1} outflow velocities traced by OH in other ULIRGs (Fischer et al. 2010; Sturm et al. 2011). Nevertheless, clear indication of outflowing gas is seen in the P-Cygni HCO$^+$ profiles observed at submillimeter wavelengths (Sakamoto et al. 2009), and is also suggested at redshifted velocities in the [O I] 145 μm line and in the low-lying OH and H$_2$O emission component profiles (Paper I).

The above independent estimates of the CR energy densities in Arp 220, and the signatures of outflowing molecular gas with low-moderate velocities, appear to be compatible with the scenario of a high density of cosmic rays producing the observed molecular ions. Papadopoulos (2010) has proposed that very high cosmic ray energy densities, of the order of those we derive here, can turn the bulk of the nuclear molecular gas in ULIRGs into giant CR-dominated Regions (CRDRs) rather than ensembles of Photon-dominated Regions (PDRs). In this framework, the O-bearing cations can be considered excellent tracers of these regions.

The case of NGC 4418 is unclear. This highly buried (Spoon et al. 2001, 2007) and highly excited (Paper I) source, where the bulk of the luminosity arises from a very small volume, is deficient in synchrotron emission with respect to the far-infrared emission (Roussel et al. 2003). Furthermore, we did not find spectroscopic signatures of outflowing gas; on the contrary the far-IR lines observed with PACS are narrow (Paper I). Therefore, cosmic rays may only be of secondary importance. An explanation of the synchrotron deficit based on a nascent starburst (Roussel et al. 2003) can hardly account for the excited OH$^+$ detected in the source, though observations of excited OH$^+$ in Galactic and other extragalactic sources are needed to check this point. Preliminarily, NGC 4418 is better interpreted as a buried AGN, and the molecular ions as produced in a XDR. But given that Arp 220 can be considered as a scaled-up version of NGC 4418, and that the columns of the cations are found similar in the nuclear regions of both sources, the possible XDR nature of Arp 220 is not ruled out.

While both NGC 4418 and Arp 220 are underluminous in hard ($2-10$ keV) X-rays for their computed SFRs (Maiolino et al. 2003; Iwasawa et al. 2005), the X-ray *absolute* fluxes may suffice to produce the inferred ionization rate. The distance-corrected X-ray fluxes of 0.1 and 0.5 erg s^{-1} cm^{-2} estimated at the surface of the nuclear regions in NGC 4418 and Arp 220 (Paper I), respectively, are lower limits due to foreground absorption in both galaxies (with $N_H \sim 10^{23}$ cm^{-2}, Paper I) and by the molecular shell itself where the ions reside. Depending on the X-ray spectrum, *local* (i.e. unattenuated) X-ray fluxes of $\gtrsim 0.5$ erg s^{-1} cm^{-2} may well produce ζ in excess of 10^{-13} s^{-1}.

The strong high-ionization Fe K line in Arp 220 (Iwasawa et al. 2005) appears to indicate that the faint X-ray emission is not primarily due to high-mass X-ray binaries (as in starburst galaxies), but could arise either from an internally shocked hot bubble of starburst origin (the pressure of which would produce the observed molecular outflow), or from a deeply embedded supermassive black hole (Iwasawa et al. 2009). In the latter case, the molecular ions would then be formed in (somewhat extended) regions that are illuminated by X-rays from the AGN that can escape to the outer (nuclear) regions primarily through inhomogeneities in the nuclear media. The drawback of this alternative is that the far-IR molecular lines are observed in absorption against dust emission that is optically thick even at far-IR wavelengths, and thus the X-ray emission from a putative buried AGN would then be strongly attenuated in arriving at such nuclear, but "surface" regions unless some special geometry is invoked[11]. Further theoretical and observational studies are required to discriminate between CRDRs and XDRs.

5.3. H_3O^+: formation pumping or hot gas?

We show in Appendix B that the H_3O^+ population diagram for the PIMS lines in Arp 220 can be understood in terms of formation pumping described by $T_{form} \sim 1000$ K, but that plausible collisional relaxation and the lack of knowledge of collisional rates make the case uncertain. Interestingly, detailed chemical models of PDRs (Hollenbach et al. 2012) predict that H_3O^+ is primarily formed in fully molecular regions, while both OH^+ and H_2O^+ peak closer to the PDR surface where f_{H_2} is significantly lower than unity. On the contrary, in Arp 220, the H_3O^+ PIMS lines peak at the redshifted velocity (LE) component (Fig. 6), which is expected to be more widespread and less dense than the blueshifted velocity (HE) component.

Nevertheless, it is worth noting that Rangwala et al. (2011) have detected high-J rotational lines of CO, which the authors interpreted as arising from hot ($\sim 10^3$ K), low density ($\sim 10^3$ cm^{-3}) gas that is mechanically heated. If the H_3O^+ lines are formed in the same region as the CO lines, the presence of such a hot molecular gas layer in Arp 220 may indeed suggest that *both* formation pumping *and* high T_{gas} are responsible for the observed PIMS absorption. Due to the low gas density associated with the redshifted (LE) component, inefficient cooling may keep the gas at high T_{gas}, which has the additional effect of boosting the H_3O^+ abundance (Fig. 11). On the other hand, the nuclear gas associated with the blueshifted velocity (HE) component is dense, and gas-grain thermal coupling (Goldsmith 2001) may be efficient in cooling the gas to the inferred $150-200$ K (based on NH$_3$ lines, Fig. 9b). Collisional relaxation of the H_3O^+ metastable populations may proceed efficiently at this T_{gas} (Fig. B.1).

---

[11] The extinction in the X-ray regime for $E_X < 10$ keV is higher than at 200 μm for a gas-to-dust ratio of 100 by mass (e.g. Montmerle 2001).

For a density of 10^4 cm^{-3} and $\zeta = 10^{-13}$ s^{-1}, the expected T_{gas} is ~ 300 K and rises very steeply with increasing ζ (Bayet et al. 2011); this result suggests X/cosmic ray heating may be important, together with mechanical heating, in explaining T_{gas} in the nuclear regions of NGC 4418 and Arp 220.

6. Conclusions

The observational results on OH^+, H_2O^+, and H_3O^+ in NGC 4418 and Arp 220 are:

– Absorption lines from excited levels of OH^+ with E_{lower} up to 285 K are detected in NGC 4418 and Arp 220. While the highest-lying lines have similar strengths in both sources, the low-lying lines are more prominent in Arp 220.
– Lines of H_2O^+ are also well detected in absorption in Arp 220 up to a lower level energy of ~ 200 K, with strong absorption in the ground-state p-H_2O^+ transition at $183-184$ μm. In contrast, in NGC 4418 the ground-state line is not detected and only several of the excited lines are detected with relatively low signal-to-noise.
– The pure-inversion, metastable lines of H_3O^+ are detected in Arp 220 up to a lower level of ~ 1400 K, indicating a rotational temperature of ~ 550 K. These lines are not detected in NGC 4418. However, the rotation-inversion lines, some of them arising from non-metastable levels, are detected in both sources.
– We identify two main velocity components in Arp 220 separated by ≈ 75 km s^{-1}. The high-lying lines of all neutral (H_2O, OH, NH$_3$, HCN) and ionized (OH^+, H_2O^+) molecular species peak at the blueshifted component, while the lowest-lying lines peak at the redshifted one. The exception corresponds to the pure-inversion metastable lines of H_3O^+, which also peak at the velocity of the redshifted component. The blueshifted line components may be tracing the outflow shown in the millimeter lines of HCO$^+$ by Sakamoto et al. (2009), and grain mantle evaporation, sputtering, and neutral-neutral reactions at high T_{gas} may all be contributing to enhance the gas-phase abundances of H_2O and NH$_3$.

The observations are analyzed with radiative transfer modeling. The conclusions stemming from the analysis are:

– The excited lines of OH^+ and H_2O^+, and the rotation-inversion lines of H_3O^+ are pumped through absorption of far-IR radiation emitted by dust, but the pure-inversion metastable lines of H_3O^+ are either chemically and/or collisionally pumped.
– OH^+ column densities of $(0.5-1.1) \times 10^{16}$ cm^{-2} are derived toward the nuclear region of both sources for spatial extents of $20-30$ pc in NGC 4418, and $90-160$ pc in Arp 220. The estimated abundance is $(1-3) \times 10^{-8}$ in both sources. In addition, in Arp 220, absorption from an extended region is required to match the low-lying OH^+ lines, with an estimated column of a few $\times 10^{16}$ cm^{-2} and an abundance of several $\times 10^{-8}$.
– The nuclear columns of H_2O^+ are $(0.3-0.9) \times 10^{16}$ cm^{-2} in Arp 220, and $(0.3-0.4) \times 10^{16}$ cm^{-2} in NGC 4418, indicating OH^+/H_2O^+ ratios of $1-2.5$ (the lower value applies to Arp 220). In Arp 220, the emission lines detected with SPIRE indicate an additional extended region with columns of several $\times 10^{15}$, similar to the column derived from the ground-state p-H_2O^+ lines, indicating a OH^+/H_2O^+ ratio of $5-10$ in the extended region.

- The H$_3$O$^+$ lines indicate columns of $(0.5-0.8) \times 10^{16}$ cm^{-2} in NGC 4418, and $(1-2) \times 10^{16}$ cm^{-2} in Arp 220. In Arp 220, the observed high excitation of the pure-inversion metastable lines may be due to both formation pumping and high T_{gas}, and the H$_3$O$^+$ lines are likely tracing a nuclear transition region into the more extended, low excitation gas. It is suggested that collisional relaxation of the H$_3$O$^+$ metastable populations is important in the dense nuclear gas of Arp 220. The H$_3$O$^+$ lines are redshifted relative to the high-lying lines of OH$^+$ with uncertain velocity overlap, and we estimate a OH$^+$/H$_3$O$^+$ ratio of ~1 in the nuclear region of both sources.

Simple chemical models are used to interpret the results of radiative transfer modeling. Our main conclusions are:

- The sequence H$^+$ → O$^+$ → OH$^+$ → H$_2$O$^+$ → H$_3$O$^+$ is favored as the primary route to explain the high columns of the O-bearing molecular ions toward the nuclear region of both sources.
- The production of H$^+$ is most probably dominated by X/cosmic ray ionization, rather than by FUV/chemical means (Appendix C). An ionization rate per hydrogen nuclei density of $\zeta/n_{\mathrm{H}} \sim (1-2) \times 10^{-17}$ cm^3 s^{-1} is estimated in the nuclei of both galaxies.
- The full set of observations and models lead us to propose that the molecular ions arise in a relatively low-density interclump medium but with density of at least 10^4 cm^{-3}, in which case the ionization rate is $\zeta > 10^{-13}$ s^{-1}, a lower limit that is over two orders of magnitude greater than the highest current rate estimates of several $\times 10^{-16}$ s^{-1} for Galactic regions.
- The cosmic-ray energy density inferred in Arp 220 from both the supernova rate and synchrotron radio emission is ~10^3 times the Galactic value (Persic & Rephaeli 2012), which is compatible with the lower limit found for ζ from the present observations and analysis. Nevertheless, an important contribution due to X-ray ionization in Arp 220 is also plausible. In NGC 4418, an XDR is favored. Further theoretical and observational studies are required to discriminate between X-ray and cosmic ray ionization.

Appendix A: Excitation of OH$^+$ and H$_2$O$^+$ through formation pumping

Here we show that formation pumping is not important for the OH$^+$ and H$_2$O$^+$ level population distribution or absorption line fluxes in Arp 220 and NGC 4418. The effect of formation pumping on the excitation of OH$^+$ can be estimated from the statistical equilibrium equations by Bruderer et al. (2010b)

(Eqs. (B1)−(B3) in their Appendix B), by ignoring the collisional and induced emission terms:

$$\frac{\mathrm{d}n_{N,J}}{\mathrm{d}t} = \sum_{J'} n_{N+1,J'} A_{N+1,J';N,J} - n_{N,J} \sum_{J'} A_{N,J;N-1,J'} + \Gamma_{N,J} - n_{N,J}\Lambda_{N,J} = 0, \tag{A.1}$$

where $A_{N,J;N',J'}$ is the Einstein coefficient for spontaneous emission from level (N, J) to level (N', J'), and $\Gamma_{N,J}$ (cm^{-3} s^{-1}) and $\Lambda_{N,J}$ (s^{-1}) are the chemical formation and destruction rates. The total OH$^+$ formation rate is

$$\Gamma_{\mathrm{OH}^+} = \sum_{N,J} \Gamma_{N,J} = n_{\mathrm{H}} \epsilon_{\mathrm{OH}^+} \zeta, \tag{A.2}$$

where ζ is the ionization rate and ϵ_{OH^+} is the efficiency with which ionizations are transfered to OH$^+$ production. The destruction rate $\Lambda_{N,J}$ is assumed to be independent of the considered level (Bruderer et al. 2010b), and for OH$^+$ is given by

$$\Lambda_{N,J} = \Lambda_{\mathrm{OH}^+} = n_{\mathrm{H}} \left(\chi_e k_{\mathrm{OH}^+|e} + 0.5 f_{\mathrm{H}_2} k_{\mathrm{OH}^+|\mathrm{H}_2} \right). \tag{A.3}$$

In steady state, $\Lambda_{\mathrm{OH}^+} = \Gamma_{\mathrm{OH}^+}/(n_{\mathrm{H}}\chi_{\mathrm{OH}^+})$, which is expected to be $<10^{-5}$ s^{-1}. Since this value is much lower than the $A_{N,J;N',J'}$ values ($\gtrsim 0.05$ s^{-1}, Table 1), the OH$^+$ molecules are destroyed once they are in the ground $(N, J) = (0, 1)$ level, and Eq. (A.1) yields for excited $N > 0$ levels

$$n_{N,J} \sum_{J'} A_{N,J;N-1,J'} = \Gamma_{N,J} + \sum_{J'} n_{N+1,J'} A_{N+1,J';N,J}. \tag{A.4}$$

For the ground $(N, J) = (0, 1)$ level we can write:

$$n_{0,1}\Lambda_{\mathrm{OH}^+} = \Gamma_{0,1} + \sum_{J'} n_{1,J'} A_{1,J';0,J}. \tag{A.5}$$

Equations (A.4) and (A.5) are easily solved iteratively by starting from a high N-level down to the $N = 0$ state. Results show that for $\chi_{\mathrm{OH}^+} \gtrsim 10^{-8}$, $\zeta < 10^{-12}$ s^{-1}, and $\epsilon_{\mathrm{OH}^+} \sim 0.5$, the three $N = 1 \rightarrow 0$ components have an excitation temperature $T_{\mathrm{ex}} < 7$ K, implying that less than 0.3% of OH$^+$ molecules are in excited levels. Therefore, excitation by dust emission is much more efficient than formation pumping in these sources. A similar analysis was done for H$_2$O$^+$, with also similar results: $T_{\mathrm{ex}} \lesssim 7$ K for the ground state transitions, and less than 1.5% of H$_2$O$^+$ molecules in excited levels.

The flux predicted in the OH$^+$ $N \rightarrow N - 1$ transition as derived from formation pumping alone can also be easily estimated. By summing over all J-levels in Eq. (A.4), one obtains

$$\sum_{J,J'} n_{N,J} A_{N,J;N-1,J'} = \sum_{N' \geq N} \sum_{J} \Gamma_{N',J}, \tag{A.6}$$

thus the number of $N \rightarrow N - 1$ line photons emitted per unit volume and time is equal in steady state to the accumulated formation rate in all $N' \geq N$ levels, and is independent of the A_{ul}−values. Writing the volume of the emitting region as $V = \pi R^2 N_{\mathrm{H}}/n_{\mathrm{H}}$, where N_{H} and n_{H} are the column and density of H nuclei, respectively, and R is the effective radius of the region, the flux in the $N \rightarrow N - 1$ fine-structure lines due to formation pumping is given by

$$F_{N \rightarrow N-1} = \frac{h\nu_{N \rightarrow N-1} R^2 N_{\mathrm{H}}}{4 n_{\mathrm{H}} D^2} \times \sum_{N' \geq N} \sum_{J} \Gamma_{N',J}, \tag{A.7}$$

where D is the distance to the source. The double sum in Eq. (A.7) is evidently lower than the total OH$^+$ formation rate (Γ_{OH^+}), and then

$$F_{N\rightarrow N-1} < \frac{h\nu_{N\rightarrow N-1}R^2 N_H \Gamma_{OH^+}}{4n_H D^2}, \qquad (A.8)$$

and using Eq. (A.2),

$$F_{N\rightarrow N-1} < \frac{h\nu_{N\rightarrow N-1}R^2 N_H \epsilon_{OH^+}\zeta}{4D^2}$$

$$\sim 1.3\times 10^{-23}\epsilon_{OH^+}\left(\frac{150\,\mu m}{\lambda}\right)\left(\frac{R}{50\,pc}\right)^2\left(\frac{72\,Mpc}{D}\right)^2$$

$$\times\left(\frac{N_H}{4\times 10^{23}\,cm^{-2}}\right)\left(\frac{\zeta}{2\times 10^{-13}\,s^{-1}}\right)\,W\,cm^{-2}. \quad (A.9)$$

The reference value is $\sim$500 times lower than the absorbing flux of the $N = 2 \leftarrow 1$ transition in Arp 220 (Table 1), indicating that formation pumping has a negligible effect on the observed line fluxes. For NGC 4418, the upper limit is 3×10^{-23} W cm^{-2} for $R = 20$ pc, also much lower than observed.

Appendix B: Excitation of H$_3$O$^+$ through formation pumping

As discussed in Sect. 3.1, the rates for H$_3$O$^+$ excitation through collisions are unknown and therefore the excitation mechanism of the high metastable levels cannot currently be determined. Nevertheless, here we attempt to constrain under what conditions formation pumping can account for the observed excitation. By assuming a range of reasonable collisional excitation rates and some simplifying but illustrative assumptions, we show here that formation pumping can play an important role in populating the highly excited metastable levels from which absorption is observed in Arp 220.

We assume that the formation distribution can be described by a formation temperature, T_{form}, so that the formation rate Γ_i in level i is (Bruderer et al. 2010b):

$$\Gamma_i = \Gamma_{H_3O^+}\times\frac{g_i\exp\{-E_i/T_{form}\}}{Q(T_{form})}, \qquad (B.1)$$

where $\Gamma_{H_3O^+}$ is the total H$_3$O$^+$ formation rate, g_i and E_i are the degeneracy and energy of level i, respectively, and Q is the partition function. H$_3$O$^+$ is expected to be formed through H$_2$O$^+$ + H$_2 \rightarrow$ H$_3$O$^+$ + H, with an exothermicity of 1.7 eV. Imposing equal momentum of the products in the rest frame, and assuming energy equipartition of H$_3$O$^+$ between rotational, vibrational, and translational energy, we roughly estimate that $\sim$0.08 eV per formed H$_3$O$^+$ molecule will go into rotational energy, implying $T_{form} \sim 800$ K. We adopt in the following $T_{form} = 1000$ K.

After a molecule is formed in a J_K^p level, it will cascade down very quickly to the metastable K_K^+ one, where it will remain until a collisional event induces a transition to another level, or until the molecule is destroyed through recombination with an electron. If the latter process dominates, the population in the metastable levels will be determined by the formation process. However, the rotational temperature T_{rot} of the metastable levels will be lower than T_{form}, because the former is determined by the *J-accumulated* formation rates in the different K-ladders. In Fig. B.1a, the colored symbols show the expected population diagram obtained by ignoring collisional relaxation. While there is not a unique T_{rot}, there is a tendency for it to increase
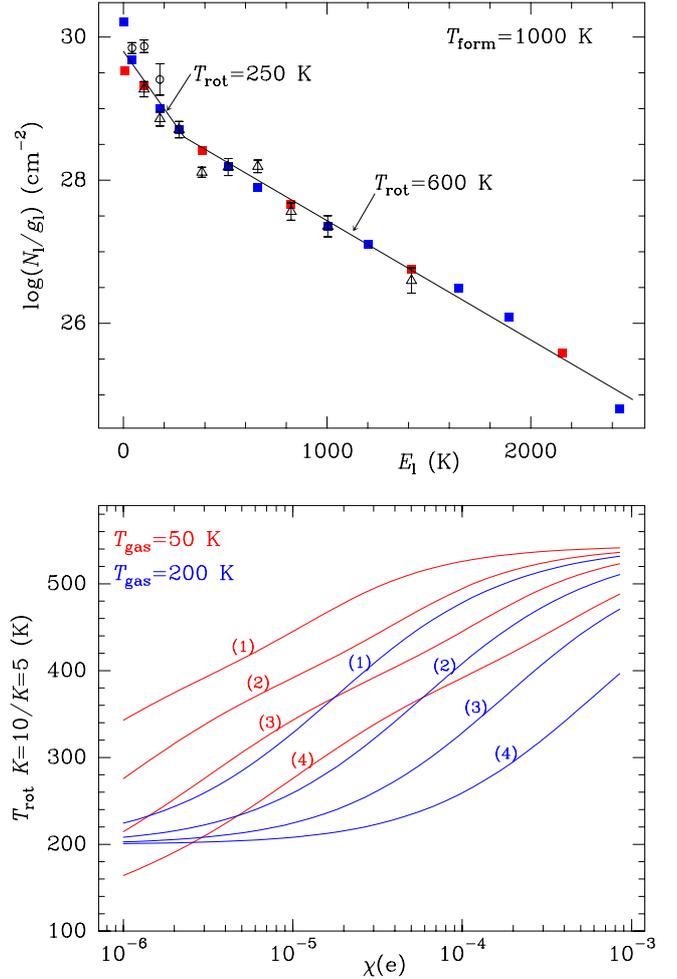
Fig. B.1. a) The H$_3$O$^+$ rotation diagram (triangles), calculated in the optically thin limit. The colored squares (red: ortho, blue: para) show the expected column density distribution for a formation temperature of T_{form} = 1000 K, and neglecting collisional relaxation. The two solid lines correspond to rotational temperatures of T_{rot} = 250 and 600 K. **b)** The rotational temperature of the 10_{10}^+ metastable level of H$_3$O$^+$ relative to the 5_5^+ one as a function of the electron abundance $\chi(e)$ for two adopted values of T_{gas} (50 and 200 K) and four assumed values of $k_{K,K'}^{col}$ = 3×10^{-11} (curves 1), 1×10^{-10} (2), 3×10^{-10} (3), and 1×10^{-9} cm^3 s^{-1} (4).

with E_l, and the expected distribution can be roughly fitted with $T_{rot} \sim 250$ and $\sim$600 K for $E_l \lesssim 300$ K and $E_l > 300$ K, respectively. This resembles the double distribution found by Lis et al. (2012) toward Sgr B2. The triangles in Fig. B.1a show the columns obtained toward Arp 220 by assuming that the observed lines are optically thin (Sect. 2.3).

In order to check under which conditions the formation process can generate the observed high excitation of the metastable H$_3$O$^+$ levels in environments with moderate T_{gas}, we have made calculations for the equilibrium populations n_K of the metastable levels by solving the rate equations

$$\frac{dn_K}{dt} = \Gamma_K + n_H\sum_{K'}n_{K'}k_{K',K}^{col}$$

$$-n_K n_H\left(\sum_{K'}k_{K,K'}^{col} + \chi_e k_{H_3O^+|e}\right) = 0, \qquad (B.2)$$

where Γ_K denotes the accumulated formation rate in all levels of the K-ladder. The rate coefficient for H$_3$O$^+$ destruction through

recombination is taken from the UMIST06 database ([Woodall et al. 2007](#)):

$$k_{\mathrm{H_3O^+|e}} = 4.32 \times 10^{-7} \times \left(\frac{T_{\mathrm{gas}}}{300\,\mathrm{K}}\right)^{-1/2} \mathrm{cm^3\ s^{-1}}. \tag{B.3}$$

We treat the collisional relaxation in a rather simplistic, but still illustrative way: only collisions between a given metastable level and the neighboring upper and lower (ortho or para) metastable levels are considered, with an effective rate of collisional de-excitation from level K to level K' given by $n_{\mathrm{H}} k_{K,K'}^{\mathrm{col}}$, assumed independent of K. The excitation rate is fixed by the requirement of detailed balance at the adopted T_{gas}.

We solved Eqs. ([B.2](#)) for all metastable levels by assuming an H₃O⁺ ortho-to-para abundance ratio of 1, and for four adopted values of $k_{K,K'}^{\mathrm{col}}$: 3×10^{-11}, 1×10^{-10}, 3×10^{-10}, and 1×10^{-9} cm³ s⁻¹. In steady state, $\Gamma_K \propto n_{\mathrm{H}}$ and under our simple assumptions the T_{rot} values are independent of n_{H}. As an example of this approach, Fig. [B.1](#)b shows the T_{rot} value between the $K = 10$ and $K = 5$ metastable levels as a function of χ_e. We adopt here $T_{\mathrm{gas}} = 50$ and 200 K, much lower than 500 K. Since both the recombination rate increases, and $k_{K,K'}^{\mathrm{col}}$ is expected to decrease with decreasing T_{gas}, we may expect the effect of formation pumping and T_{rot} to be the highest for the *lowest* T_{gas}. For $T_{\mathrm{gas}} = 50$ K, T_{rot} is much higher than T_{gas} even for relatively low $\chi_e \sim 10^{-6}$. $T_{\mathrm{rot}} \sim 500$ K is then obtained for $\chi_e \sim 10^{-4}$, typical of translucent clouds, provided that $k_{K,K'}^{\mathrm{col}} \lesssim 10^{-10}$ cm³ s⁻¹. Higher $T_{\mathrm{gas}} = 200$ K implies a lower recombination rate and a presumably higher $k_{K,K'}^{\mathrm{col}}$, with the consequence that T_{rot} decreases for the same χ_e. From the excitation point of view, we thus roughly expect two *opposite* solutions to explain $T_{\mathrm{rot}} \gtrsim 500$ K as observed in Arp 220: low T_{gas} ($\lesssim 100$ K) and, of course, high $T_{\mathrm{gas}} \gtrsim 500$ K.

Appendix C: The formation and abundance of OH⁺

Here we present the full set of calculated abundances of OH⁺, H₂O⁺, and H₃O⁺, together with the corresponding abundances of electrons and H⁺, based on the methods discussed in Sect. 4. Some analytical expressions for OH⁺ production rates are compared, showing that the most likely path for OH⁺ formation is O⁺ + H₂, with the contribution from the charge exchange reaction H⁺ + OH and from direct OH ionization being of secondary importance even in the nuclear regions, where high OH abundances are inferred (Paper I). We also show that H⁺ is most likely formed through X/cosmic ray ionization, rather than via the C⁺ + OH → CO⁺ + H → CO + H⁺ FUV/chemical path.

The predicted OH⁺ abundance relative to H nuclei, $\chi_{\mathrm{OH^+}}$, and both R_1 and R_2 are shown in Fig. [C.1](#) as a function of $f_{\mathrm{H_2}}$ for several values of ζ/n_{H}, together with the values inferred in the nuclear regions of NGC 4418 and Arp 220 (shaded dark regions) and in the C_{extended} of Arp 220 (shaded light regions). The abundances of H⁺ and e⁻ are also shown in the lower panel.

The values relevant to the nuclear regions, $\chi_{\mathrm{OH^+}} = (1-3) \times 10^{-8}$, $R_1 \sim 1-2.5$, and $R_2 \sim 1$, can be obtained for very different values of ζ/n_{H}, provided that $f_{\mathrm{H_2}}$ attains the appropriate regime. For example, values compatible with observations are found for $\zeta/n_{\mathrm{H}} \approx 5 \times 10^{-19}$ cm³ s⁻¹, $f_{\mathrm{H_2}} \approx 0.1$, and high T_{gas}. For low values of ζ/n_{H}, however, the range of $f_{\mathrm{H_2}}$ compatible with observations is very narrow. This range broadens for higher ζ/n_{H} and $f_{\mathrm{H_2}}$, which we favor owing to the inferred high column densities.

According to the equilibrium $\chi_{\mathrm{H^+}}$ and χ_e, we can compare the OH⁺ volume formation rates due to O⁺ + H₂, $\Gamma_{\mathrm{OH^+;O^+|H_2}}$, and
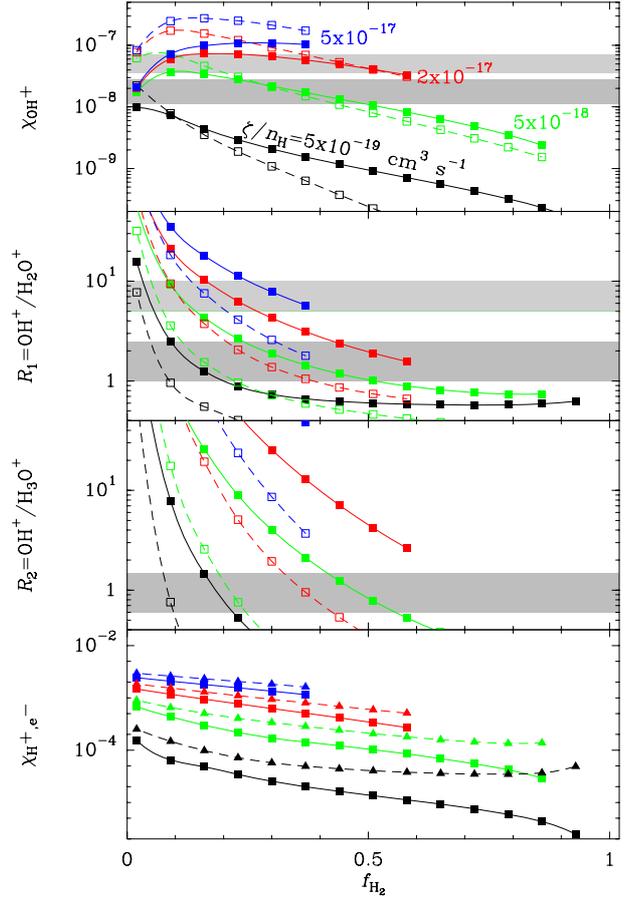
Fig. C.1. Predicted OH⁺ abundance (*upper panel*), OH⁺/H₂O⁺ and OH⁺/H₃O⁺ ratios (*mid panels*), and H⁺ and e⁻ abundances (*lower panel*), as a function of the molecular fraction $f_{\mathrm{H_2}}$ (up to approximately $f_{\mathrm{H_2}}^{\mathrm{max}}$, see Eq. ([2](#))). Each curve corresponds to a value of ζ/n_{H}, indicated in the *upper panel* in units of cm³ s⁻¹. Solid and dashed curves correspond to $T_{\mathrm{gas}} = 150$ and 550 K, respectively. The inferred values of $\chi_{\mathrm{OH^+}}$, R_1, and R_2, in the nuclear regions of NGC 4418 and Arp 220, and in the C_{extended} of Arp 220, are indicated with the shaded dark and light regions, respectively. In the *lower panel*, squares and triangles show the predicted $\chi_{\mathrm{H^+}}$ and χ_e.

due to O + H₃⁺, $\Gamma_{\mathrm{OH^+;H_3^+|O}}$, at high $f_{\mathrm{H_2}}$ (see [Liszt 2007](#), for diffuse clouds). In what follows, $k_{\mathrm{X|Y}}$ is the rate coefficient for the X + Y reaction. On the one hand, $\Gamma_{\mathrm{OH^+;O^+|H_2}} = 0.5 f_{\mathrm{H_2}} n_{\mathrm{H}}^2 \chi_{\mathrm{O^+}} k_{\mathrm{O^+|H_2}}$, where $\chi_{\mathrm{O^+}} \approx k_{\mathrm{H^+|O}} \chi_{\mathrm{O^0}} \chi_{\mathrm{H^+}} (0.5 f_{\mathrm{H_2}} k_{\mathrm{O^+|H_2}} + (1 - f_{\mathrm{H_2}}) k_{\mathrm{O^+|H}})^{-1}$. Using the UMIST06 reactions rates given in Table [C.1](#) at $T_g = 150$ K,

$$\Gamma_{\mathrm{OH^+;O^+|H_2}} \approx 2.5 \times 10^{-18} \times n_{\mathrm{H}}^2 \times \frac{1}{1 + 0.55(1 - f_{\mathrm{H_2}})/f_{\mathrm{H_2}}}$$

$$\times \frac{\chi_{\mathrm{O^0}}}{3 \times 10^{-4}} \times \frac{\chi_{\mathrm{H^+}}}{6 \times 10^{-5}}\ \mathrm{cm^{-3}\ s^{-1}}. \tag{C.1}$$

On the other hand, $\Gamma_{\mathrm{OH^+;H_3^+|O}} = n_{\mathrm{H}}^2 \chi_{\mathrm{O^0}} k_{\mathrm{H_3^+|O}} \chi_{\mathrm{H_3^+}}$, where $\chi_{\mathrm{H_3^+}} \approx k_{\mathrm{H_3^+|e}}^{-1} (f_{\mathrm{H_2}}/\chi_e)(\zeta/n_{\mathrm{H}})$. Therefore,

$$\Gamma_{\mathrm{OH^+;H_3^+|O}} \approx 1.7 \times 10^{-19} \times n_{\mathrm{H}}^2 \times \frac{\chi_{\mathrm{O^0}}}{3 \times 10^{-4}}$$

$$\times \frac{f_{\mathrm{H_2}}/\chi_e}{3.3 \times 10^3} \times \frac{\zeta/n_{\mathrm{H}}}{2 \times 10^{-17}\ \mathrm{cm^3\ s^{-1}}}\ \mathrm{cm^{-3}\,s^{-1}} \tag{C.2}$$

Table C.1. Relevant reaction rates involved in the OH^+, H_2O^+, and H_3O^+ formation and destruction.

Reaction	Rate coefficient (cm^3 s^{-1})
$H^+ + O \rightarrow O^+ + H$	$k_{H^+|O} = 7.31 \times 10^{-10} \, T_{300}^{0.23} \exp\{-225.9/T\}$
$O^+ + H \rightarrow O + H^+$	$k_{O^+|H} = 5.66 \times 10^{-10} \, T_{300}^{0.36} \exp\{8.6/T\}$
$O^+ + H_2 \rightarrow OH^+ + H$	$k_{O^+|H_2} = 1.7 \times 10^{-9}$
$OH^+ + H_2 \rightarrow H_2O^+ + H$	$k_{OH^+|H_2} = 1.01 \times 10^{-9}$
$H_2O^+ + H_2 \rightarrow H_3O^+ + H$	$k_{H_2O^+|H_2} = 6.4 \times 10^{-10}$
$H^+ + OH \rightarrow OH^+ + H$	$k_{H^+|OH} = 2.1 \times 10^{-9}$
$H^+ + H_2O \rightarrow H_2O^+ + H$	$k_{H^+|H_2O} = 6.9 \times 10^{-9}$
$H_2^+ + H_2 \rightarrow H_3^+ + H$	$k_{H_2^+|H_2} = 2.08 \times 10^{-9}$
$H_3^+ + O \rightarrow OH^+ + H_2$	$k_{H_3^+|O:OH^+} = 8.4 \times 10^{-10}$
$H_3^+ + O \rightarrow H_2O^+ + H$	$k_{H_3^+|O:H_2O^+} = 3.6 \times 10^{-10}$
$H_3^+ + OH \rightarrow H_2O^+ + H_2$	$k_{H_3^+|OH} = 1.3 \times 10^{-9}$
$H_3^+ + H_2O \rightarrow H_3O^+ + H_2$	$k_{H_3^+|H_2O} = 5.9 \times 10^{-9}$
$OH^+ + e \rightarrow O + H$	$k_{OH^+|e} = 3.75 \times 10^{-8} \, T_{300}^{-0.5}$
$H_2O^+ + e \rightarrow$ products	$k_{H_2O^+|e} = 4.3 \times 10^{-7} \, T_{300}^{-0.5}$
$H_3O^+ + e \rightarrow$ products	$k_{H_3O^+|e} = 4.3 \times 10^{-7} \, T_{300}^{-0.5}$
$H_3^+ + e \rightarrow$ products	$k_{H_3^+|e} = 6.7 \times 10^{-8} \, T_{300}^{-0.52}$

Notes. Rate coefficients are taken from the UMIST06 database (Woodall et al. 2007). $^{(a)}$ T_{300} is $T/300$ K; T denotes T_{gas}.

Taking the limit $f_{H_2} \approx 1$ in Eq. (C.1), one obtains

$$\frac{\Gamma_{OH^+;O^+|H_2}}{\Gamma_{OH^+;H_3^+|O}} \sim 15 \times \frac{\chi_e/f_{H_2}}{3 \times 10^{-4}} \times \frac{\chi_{H^+}}{6 \times 10^{-5}}$$
$$\times \frac{2 \times 10^{-17} \text{ cm}^3 \text{ s}^{-1}}{\zeta/n_H}. \quad (C.3)$$

The reference values in Eqs. (C.1)–(C.3) are based on $\zeta/n_H = 2 \times 10^{-17}$ cm^3 s^{-1} at $T_g = 150$ K, and indicate $\Gamma_{OH^+;O^+|H_2} \gg \Gamma_{OH^+;H_3^+|O}$; increasing ζ/n_H would increase both χ_{H^+} and χ_e, thus further increasing the above ratio. The $O + H_3^+$ mechanism only becomes competitive for low $\zeta/n_H \lesssim 5 \times 10^{-19}$ cm^3 s^{-1} and $f_{H_2} \approx 1$, but the resulting OH^+ abundance is then much lower than the inferred one (Fig. C.1) and the OH^+/H_2O^+ ratio becomes lower than 1 (Hollenbach et al. 2012).

In the nuclear regions of both NGC 4418 and Arp 220, high reservoirs of OH and H_2O are found, with estimated abundances $\chi_{H_2O} \sim (0.5-1) \times 10^{-5}$ and $OH/H_2O \sim 0.5$ (Paper I). The OH^+ volume formation rate due to $H^+ + OH$ is given by $\Gamma_{OH^+;H^+|OH} = n_H^2 \chi_{H^+} \chi_{OH} k_{H^+|OH}$, and so

$$\Gamma_{OH^+;H^+|OH} \approx 3.8 \times 10^{-19} n_H^2 \times \frac{\chi_{OH}}{3 \times 10^{-6}}$$
$$\times \frac{\chi_{H^+}}{6 \times 10^{-5}} \text{ cm}^{-3} \text{ s}^{-1}, \quad (C.4)$$

which is significantly lower than $\Gamma_{OH^+;O^+|H_2}$ in Eq. (C.1) if there is enough free oxygen. However, a significant fraction of O^0 in these high density regions is expected to be locked into CO, H_2O, OH and O_2. Depletion of free O^0 into molecules in regions dominated by hot core chemistry (Paper I) would thus reduce the OH^+ formation rate in Eq. (C.1), thus increasing the potential relative importance of $\Gamma_{OH^+;H^+|OH}$. There is, however, an observational drawback for the potential importance of $H^+ + OH$. The rate of H_2O^+ formation due to $H^+ + H_2O$ is higher than $\Gamma_{OH^+;H^+|OH}$, because both $\chi_{H_2O} > \chi_{OH}$ (Paper I) and $k_{H^+|H_2O} > k_{H^+|OH}$ (Table C.1). Thus, if the OH^+ were formed via

$H^+ + OH$, one would also expect an additional, important contribution to H_2O^+ formation due to $H^+ + H_2O$, and then R_1 would fall below the inferred value of $1-2.5$. Likewise, direct ionization of OH due to UV photons is expected to be of secondary importance, because H_2O has a higher cross-section for ionization. As we argue in Sect. 4.5, the observed lines of molecular ions are most probably formed in regions where the formation rate is enhanced due to the presence of high quantities of atomic oxygen, and where the ions survive sufficiently long due to the presence of moderate densities.

According to the above discussion, model results for χ_{OH^+} and R_1 relevant for the current observations can be basically understood in terms of the $H^+ \rightarrow O^+ \rightarrow OH^+ \rightarrow H_2O^+ \rightarrow H_3O^+$ sequence, but how is the H^+ produced? We have been assuming in the analysis that the H^+ ionization is caused by X/cosmic rays, but the possibility of enhanced H^+ production by chemical routes, as discussed by Sternberg & Dalgarno (1995) and Hollenbach et al. (2012), is worth considering. According to their models for high density PDRs illuminated by strong FUV fields, in the hot transition region between the H I and H_2 zones, a major source of H^+ formation is given by $OH + C^+ \rightarrow CO^+ + H$ followed by $CO^+ + H \rightarrow CO + H^+$. OH would be produced via the endothermic $O + H_2 \rightarrow OH + H$, that is enhanced provided that a fraction of H_2 is vibrationally excited. The volume rate of H^+ production is given by $\Gamma_{H^+;OH|C^+} = n_H^2 k_{OH|C^+} \chi_{OH} \chi_{C^+} (1 + \alpha)^{-1}$, where α stands for the chance that CO^+ reacts with H_2 rather than with H I. In the limit $\alpha = 0$, and using the value for $k_{OH|C^+}$ given by Hollenbach et al. (2012),

$$\Gamma_{H^+;OH|C^+} = 2 \times 10^{-18} n_H^2 \times \frac{\chi_{C^+}}{1.4 \times 10^{-4}} \times \frac{\chi_{OH}}{5 \times 10^{-6}} \text{ cm}^{-3} \text{ s}^{-1} \quad (C.5)$$

for $T_{gas} = 300$ K; the reference value for χ_{OH} is taken from Paper I. This is equivalent to a cosmic ray ionization per unit density of $\zeta/n_H \sim 2 \times 10^{-18}$ cm^3 s^{-1}, and predicts a peak of OH^+ abundance of $\sim 10^{-8}$ as well as R_1 and R_2 values of ~ 1 (Sternberg & Dalgarno 1995; Hollenbach et al. 2012), as roughly inferred in both NGC 4418 and Arp 220. This FUV/chemical route for the production of H^+ has in the present case, however, one main drawback: the nuclear OH^+ is observed over a range in visual extinction of $\Delta A_V \sim 200$ mag, while theoretical predictions indicate a peak thickness in the OH^+ abundance of $\Delta A_V < 1$ mag where C^+ is still abundant and T_{gas} remains high. It seems very unlikely that FUV radiation maintains basically all carbon ionized, and a relatively low H_2 fraction, over columns of $\Delta A_V \sim 200$ mag along the line of sight and over spatial scales of $20-30$ and $80-150$ pc in NGC 4418 and Arp 220, respectively (see also models by Abel et al. 2009). Even if 10^6 O stars were packed into a region of ~ 10 pc radius (NGC 4418), the column density between neighboring stars would be $\sim 10^{23}$ cm^{-2}, and the quickly absorbed FUV radiation would only affect relatively compact regions around the stars. In summary, the inferred columns of O-bearing cations favor a source of ionization that can penetrate through large columns of gas, indicating the importance of X and cosmic rays.

The dependence of χ_{OH^+} on both f_{H_2} and ζ/n_H in Fig. C.1 can be understood as follows. For given f_{H_2}, χ_{OH^+} scales linearly with ζ/n_H for relatively low values of ζ/n_H, but *saturates* for sufficiently high values of ζ/n_H. Saturation occurs when the destruction of OH^+ is dominated by recombination, rather than by reaction with H_2 (producing H_2O^+). In the saturated regime, further increase of ζ/n_H increases by the same factor the OH^+ formation rate and the OH^+ destruction rate per unit of OH^+ molecule, leaving χ_{OH^+} unchanged. The condition for saturation is given by $\chi_e k_{OH^+|e} \gg 0.5 f_{H_2} k_{OH^+|H_2}$, where

$k_{\text{OH}^+|\text{e}} \approx 5 \times 10^{-8}$ cm^3 s^{-1} at 150 K, and $k_{\text{OH}^+|\text{H}_2} = 10^{-9}$ cm^3 s^{-1}. The above condition yields $\chi_\text{e} \gg 10^{-2} \times f_{\text{H}_2}$. Once saturated, χ_{OH^+} can be approximated analytically by

$$\chi_{\text{OH}^+}^{\text{sat}} \approx \frac{k_{\text{H}^+|\text{O}}}{k_{\text{OH}^+|\text{e}}} \times \frac{0.5 f_{\text{H}_2} k_{\text{O}^+|\text{H}_2}}{0.5 f_{\text{H}_2} k_{\text{O}^+|\text{H}_2} + (1 - f_{\text{H}_2}) k_{\text{O}^+|\text{H}}} \times \chi_{\text{O}^0}$$

$$\approx 7.9 \times 10^{-7} \times \frac{1}{1 + 0.55(1 - f_{\text{H}_2})/f_{\text{H}_2}} \times \frac{\chi_{\text{O}^0}}{3 \times 10^{-4}} \quad (C.6)$$

giving, for $T_{\text{gas}} = 150$ K, $\chi_{\text{OH}^+}^{\text{sat}} \approx 2.7 \times 10^{-8}$ and 3.4×10^{-7} for $f_{\text{H}_2} = 0.02$ and 0.3, respectively, in rough agreement with the values in Fig. C.1.

The dependence of χ_{OH^+} on f_{H_2} is different in the saturated and unsaturated regimes. According to Eq. (C.6), χ_{OH^+} increases with f_{H_2} in the saturated regime, because the O$^+$ + H$_2$ reaction producing OH$^+$ is increasingly favored relative to O$^+$ + H, which transfers the charge back to atomic hydrogen. However, in the unsaturated regime χ_{OH^+} *decreases* with increasing f_{H_2} (Fig. C.1). In this case, OH$^+$ destruction is dominated by OH$^+$ + H$_2$ and χ_{OH^+} is thus analitically aproximated as

$$\chi_{\text{OH}^+}^{\text{unsat}} \approx \frac{k_{\text{H}^+|\text{O}}}{k_{\text{OH}^+|\text{H}_2}} \times \frac{k_{\text{O}^+|\text{H}_2} \chi_{\text{H}^+}}{0.5 f_{\text{H}_2} k_{\text{O}^+|\text{H}_2} + (1 - f_{\text{H}_2}) k_{\text{O}^+|\text{H}}} \times \chi_{\text{O}^0}$$

$$\approx 1.5 \times 10^{-8} \times \frac{1}{1 + 0.82 f_{\text{H}_2}} \times \frac{\chi_{\text{O}^0}}{3 \times 10^{-4}} \times \frac{\chi_{\text{H}^+}}{10^{-4}}. \quad (C.7)$$

Therefore, $\chi_{\text{OH}^+}^{\text{unsat}}$ decreases with increasing f_{H_2}. For given ζ/n_H (i.e. for each curve in Fig. C.1), a maximum of OH$^+$ is reached between the saturated regime (low f_{H_2}) and the unsaturated one (high f_{H_2}).

References

Aalto, S., Costagliola, F., van der Tak, F., & Meijerink, R. 2011, A&A, 527, 69
Abdo, A. A., Ackermann, M., Ajello, M., et al. 2010, ApJ, 709, L152
Abramowski, A., et al. (H.E.S.S. Collaboration) 2012, ApJ, 757, 158
Acero, F. (H.E.S.S. Collaboration) et al. 2009, Science, 326, 1080
Acciari, V. A., et al. (VERITAS Collaboration) 2009, Nature, 462, 770
Batejat, F., Conway, J. E., Hurley, R., et al. 2011, ApJ, 740, 95
Bayet, E., Williams, D. A., Hartquist, T. W., & Viti, S. 2011, MNRAS, 414, 1583
Bekooy, J. P., Verhoeve, P., Meerts, W. L., & Dymanus, A. 1985, J. Chem. Phys. 82, 3868
Botschwina, P., Rosmus, P., & Reinsch, E. A. 1985, Chem. Phys. Lett., 102, 299
Bruderer, S., Doty, S. D., & Benz, A. O. 2009, ApJS, 183, 179
Bruderer, S., Benz, A. O., Stuber, P., Doty, S. D. 2010a, ApJ, 720, 1432
Bruderer, S., Benz, A. O., van Dishoeck, E. F., et al. 2010b, A&A, 521, L44
Cazaux, S., & Tielens, A. G. G. M. 2004, ApJ, 604, 222
Cuppen, H. M., Kristensen, L. E., & Gavardi, E. 2010, MNRAS, 406, L11
Doty, S. D., van Dishoeck, E. F., van der Tak, F. F. S., & Boonman, A. M. S. 2002, A&A, 389, 446
Downes, D., & Eckart, A. 2007, A&A, 468, L57
Engelbracht, C. W., Rieke, M. J., Rieke, G. H., Kelly, D. M., & Achtermann, J. M. 1998, ApJ, 505, 639
Faure, A., & Tennyson, J. 2003, MNRAS, 340, 468
Fischer, J., Sturm, E., González-Alfonso, E., et al. 2010, A&A, 518, L41
Gerin, M., de Luca, M., Black, J., et al. 2010, A&A, 518, L110
Goldsmith, P. F. 2001, ApJ, 557, 736
González-Alfonso, E., & Cernicharo, J. 1999, ApJ, 525, 845
González-Alfonso, E., Smith, H. A., Fischer, J., & Cernicharo, J. 2004, ApJ, 613, 247 (G-A04)
González-Alfonso, E., Smith, H. A., Ashby, M. L. N., et al. 2008, ApJ, 675, 303
González-Alfonso, E., Fischer, J., Graciá-Carpio, J., et al. 2012, A&A, 541, A4 (Paper I)
Gupta, H., Rimmer, P., Pearson, J. C., et al. 2010, A&A, 521, L47
Graciá-Carpio, Sturm, E., Hailey-Dunsheath, S., et al. 2011, ApJ, 728, L7

Haas, M., Klaas, U., Müller, S. A. H., Chini, R., & Coulson, I. 2001, A&A, 367, L9
Hailey-Dunsheath, S., Sturm, E., Fischer, J., et al. 2012, ApJ, 755, 57
Herbst, E., & Klemperer, W. 1973, ApJ, 185, 505
Hollenbach, D., Kaufman, M. J., Neufeld, D., Wolfire, M., & Goicoechea, J. R. 2012, ApJ, 754, 105
Indriolo, N., Geballe, T. R., Oka, T., & McCall, B. J. 2007, ApJ, 671, 1736
Indriolo, N., Neufeld, D. A., Gerin, M., et al. 2012, ApJ, 758, 83
Iwasawa, K., Sanders, D. B., Evans, A. S., et al. 2005, MNRAS, 357, 565
Iwasawa, K., Sanders, D. B., Evans, A. S., et al. 2009, ApJ, 695, L103
Kaufman, M. J., Wolfire, M. G., Hollenbach, D. J., & Luhman, M. L. 1999, ApJ, 527, 795
Lim, A. J., Rabadán, I., & Tennyson, J. 1999, MNRAS, 306, 473
Lis, D. C., Schilke, P., Bergin, E. A., et al. 2012, Phil. Trans. R. Soc. A, in press
Liszt, H. S. 2007, A&A, 461, 205
Lonsdale, C. J., Diamond, P. J., Thrall, H., Smith, H. E., & Lonsdale, C. J. 2006, ApJ, 647, 185
Luhman, M. L., Satyapal, S., Fischer, J., et al. 2003, ApJ, 594, 758
Maiolino, R., Comastri, A., Gilli, R., et al. 2003, MNRAS, 344, L59
Maloney, P. R., Hollenbach, D, J., & Tielens, A. G. G. M. 1996, ApJ, 466, 561
Meijerink, R., Spaans, M., Loenen, A. F., & van der Werf, P. P. 2011, A&A, 525, 119
Montmerle, T. 2001, ASP Conf. Ser., 243, 731
Müller, H. S. P., Thorwirth, S., Roth, D. A., & Winnewisser, G. 2001, A&A, 370, L49
Müller, H. S. P., Schlöder, F., Stutzki, J., & Winnewisser, G. 2005, J. Mol. Struct., 742, 215
Mürtz, P., Zink, L. R., Evenson, K. M., & Brown, J. M. 1998, J. Chem. Phys., 109, 9744
Neufeld, D. A., & Dalgarno, A. 1989, Phys. Rev. A, 40, 633
Neufeld, D. A., Goicoechea, J. R., Sonnentrucker, P., et al. 2010, A&A, 521, L10
Offer, A. R., & van Hemert, M. C. 1992, Chem. Phys., 163, 83
Ott, J., Henkel, C., Braatz, J. A., & Weiss, A. 2011, ApJ, 742, 950
Ossenkopf, V., Müller, H. S. P., Lis, D. C., et al. 2010, A&A, 518, L111
Papadopoulos, P. P. 2010, ApJ, 720, 226
Parra, R., Conway, J. E., Diamond, P. J., et al. 2007, ApJ, 659, 314
Persic, M., & Rephaeli, Y. 2012, J. Phys. Conf. Ser., 355, 012038
Pickett, H. M. 1991, J. Mol. Spectrosc., 148, 371
Pickett, H. M., Poynter, R. L., Cohen, E. A., et al. 1998, JQSRT, 60, 883
Poglitsch, A., Waelkens, C., Geis, N., et al. 2010, A&A, 518, L2
Polehampton, E. T., Baluteau, J.-P., & Swinyard, B. M., et al. 2007, MNRAS, 377, 1122
Rangwala, N., Maloney, P. R., Glenn, J., et al. 2011, ApJ, 743, 94
Roussel, H., Helou, G., Beck, R., et al. 2003, ApJ, 593, 733
Sakamoto, K., Wang, J., Wiedner, et al. 2008, ApJ, 684, 957
Sakamoto, K., Aalto, S., Wilner, D. J., et al. 2009, ApJ, 700, L104
Schilke, P., Comito, C., Müller, H. S. P., et al. 2010, A&A, 521, L11
Spoon, H. W. W., Keane, J. V., Tielens, A. G. G. M., et al. 2001, A&A, 365, L353
Spoon, H. W. W., Moorwood, A. F. M., Lutz, D., et al. 2004, A&A, 414, 873
Spoon, H. W. W., Marshall, J. A., Houck, J. R., et al. 2007, A&A, 365, L353
Stäuber, P., & Bruderer, S. 2009, A&A, 505, 195
Stäuber, P., Doty, S. D., van Dishoeck, E. F., & Benz, A. O. 2005, A&A, 440, 949
Sternberg, A., & Dalgarno, A. 1995, ApJS, 99, 565
Strahan, S. E., Müller, R. P., & Saykally, R. J. 1986, J. Chem. Phys., 85, 1252
Strickland, D. K., & Heckman, T. M., 2007, ApJ, 658, 258
Sturm, E., González-Alfonso, E., Veilleux, S., et al. 2011, ApJ, 733, L16
Sugai, H., Davies, R. I., & Ward, M. J. 2003, ApJ, 584, L9
van der Tak, F. F. S., Belloche, A., Schilke, P., et al. 2006, A&A, L99
van der Tak, F. F. S., Aalto, S., & Meijerink, R. 2008, A&A, 477, L5 (vdT08)
van der Tak, F. F. S., Ossenkopf, V., Nagy, Z., et al. 2012, A&A, 537, L10
van der Werf, P. P., Isaak, K. G., Meijerink, R., et al. 2010, A&A, 518, L42
Veilleux, S., Rupke, D. S. N., & Swaters, R., 2009, ApJ, 700, L149
Verhoeve, P., Versluis, M., ter Meulen, J. J., Meerts, W. L., & Dymanus, A. 1989, Chem. Phys. Lett., 161, 195
Weis, B., Carter, S., Rosmus, P., Werner, H.-J., & Knowles, P. J. 1989, J. Chem. Phys., 91, 2818
Weiß, A., Requena-Torres, M. A., Güsten, R., et al. 2010, A&A, 521, L1
Werner, H.-J., Rosmus, P., & Reinsch, E.-A. 1983, J. Chem. Phys., 79, 905
Woodall, J., Agúndez, M., Markwick-Kemper, A. J., & Millar, T. J. 2007, A&A 466, 1197
Wootten, A., Mangum, J. G., Turner, B. E., et al. 1991, ApJ, 380, L79
Wyrowski, F., Menten, K. M., Güsten, R., & Belloche, A. 2010, A&A, 518, 26
Yu, S., Drouin, B. J., Pearson, J. C., & Pickett, H. M. 2009, ApJS, 180, 119